Meteoric diagenesis influenced by East Asian Summer Monsoon: A case study from the Pleistocene carbonate succession, Xisha Islands, South China Sea

Lü Wu [a], Rui Wang [a,*], Kefu Yu [a,b,c,*], Min Ren [d], Simone Booker [e], Ruoxia Shen [a], Wei Jiang [a], Shendong Xu [a], Tianlai Fan [a], Songye Wu [a], Qiushuang Qin [a], Xingchi Li [a]

[a] Guangxi Laboratory on the Study of Coral Reefs in the South China Sea, Coral Reef Research Center of China, School of Marine Sciences, Guangxi University, Nanning 530004, China
[b] Southern Marine Science and Engineering Guangdong Laboratory, Zhuhai 519080, China
[c] Laboratory for Marine Geology, Qingdao National Laboratory for Marine Science and Technology, Qingdao 266061, China
[d] College of Ocean and Earth Sciences, Xiamen University, Xiamen 361005, China
[e] Department of Geology, Saint Mary's University, Halifax B3H 3H3, Canada

ARTICLE INFO

ABSTRACT

The East Asian Monsoon (EAM) has significantly influenced various depositional and diagenetic processes in carbonate sediments in much of East and South Asia during the Cenozoic. The relationship between the EAM and marine carbonate platforms, which are widely developed in this region, however, remains largely unknown. Based on petrographic, mineralogical, and geochemical analyses of the carbonate succession (~237 m thick) on the Xisha Islands, South China Sea, meteoric diagenesis and its relationship with the East Asian Summer Monsoon (EASM) during the Pleistocene were studied. Various petrographic features, stable isotopes (δ^{13}C, δ^{18}O), and trace elements (Sr, Fe, Mn, Rare Earth Elements and Y) indicate that this succession was extensively altered by meteoric diagenesis, producing four exposed surfaces embedded in the shallow coral reef sediments. Given this data, we suggest that the meteoric diagenesis that affected this succession occurred during periods of low sea-level, and was potentially related to the relative intensity of the EASM. During strong EASM periods, particularly during the Mid-Pleistocene Transition ~0.9 Ma, meteoric diagenesis was intense, as suggested by the complete alteration of unstable minerals, extreme dissolution, the presence of reddish-brown iron oxides, and a large negative excursion of δ^{13}C (−6.2‰). The influence of the EASM on meteoric diagenesis of Pleistocene carbonate platforms can be identified throughout the South China Sea. This study sheds light on the relationship between meteoric diagenesis and paleo-climate conditions in carbonate platform regions that are influenced by monsoons.

1. Introduction

The East Asian Monsoon (EAM) formed in the early Cenozoic and is a critical component of the global monsoonal system, with strong southerly winds in summer [i.e., the East Asian Summer Monsoon (EASM)], and strong northerly winds in winter [i.e., the East Asian Winter Monsoon (EAWM)] in much of South and East Asia (Ding et al., 1994; Molnar et al., 2010; Huang et al., 2012; Clift et al., 2014; Gai et al., 2020;

Zhang et al., 2022). When the EAWM prevails, the climate over East Asia is characterized by low temperatures and arid conditions, whereas when the EASM prevails, the climate over East Asia becomes wet and warm due to increased moisture and precipitation (Wan et al., 2007; Clift et al., 2014). Although research on the EAM has been acquired through the study of various geological archives such as cave stalagmites, deep-sea sediments, loess, and lake sediments, very few attempts have been made to understand the EAM in carbonate platform records (Steinke

---

et al., 2010; Jiang et al., 2018). In the South China Sea, carbonate platform deposition began during the early Miocene (Wu et al., 2021). These carbonate successions have not been investigated in relation to the EAM due to their complex diagenetic histories. Various studies, however, have shown a potential link between carbonate platforms and the EAM over long time periods (Wan et al., 2007, Zhao, 2010; Zhao et al., 2011). Li et al. (2018), for example, suggested that the Holocene carbonate rocks on the Xisha Islands were affected by dry-wet climate cycles controlled by the EAM.

Isolated carbonate platforms, such as the Xisha platform (Fig. 1A), which develop in warm, shallow, and clear near-surface marine environments with no riverine input, are expected to preserve a relatively complete and easily dated record of meteoric erosion during sea-level lowstands (Allan and Matthews, 1982; Swart, 2015; Jones, 2016; Fantle et al., 2020). The rate of meteoric diagenesis and mineral alteration in carbonate platform sediments is largely associated with the volume of rainfall input (Li et al., 2018) and is several times higher in humid climates than in arid climates (Matthews, 1968; Harrison, 1975; Christl et al., 2012). Chemical weathering, therefore, on platform tops should be closely related to humid periods, such as those in which the EASM prevails. In fact, in the South China Sea, most of the annual rainfall

occurs during the summer monsoon season (85–90%) (Liu et al., 2007). Multi-stage exposure surfaces with iron oxide, karst-dissolved pores, and calcareous laterites related to meteoric diagenesis have been identified on the Xisha Islands (Liu et al., 1998a; Chen et al., 2020) and Nansha Islands (Luo et al., 2022) in the South China Sea during the Pleistocene. Unfortunately, many of these studies focused on single monsoon events or meteoric diagenesis in modern and Holocene carbonates (Rea et al., 1998; Hongbo et al., 2000; Jian et al., 2003; Huang et al., 2003; Huang et al., 2005; Fantle et al., 2020). In this study, however, we suggest that the meteoric diagenesis that affected the carbonate platform of the Xisha Islands could have been influenced by the intensity of EASM during the Pleistocene.

In 2013, well Chenke-2 (CK-2) was drilled on the isolated Xisha Islands, and a relatively complete Pleistocene carbonate secession was obtained (average recovery rate > 70%), providing high quality materials for studying the relationship between EASM and carbonate meteoric diagenesis. Here, our research presents petrological, mineralogical, and geochemical data from the carbonate succession of well CK-2 on the Xisha Islands in the South China Sea to provide insights on the 1) meteoric diagenesis of the Xisha platform during the Pleistocene and 2) potential link between meteoric diagenesis and EASM intensity.
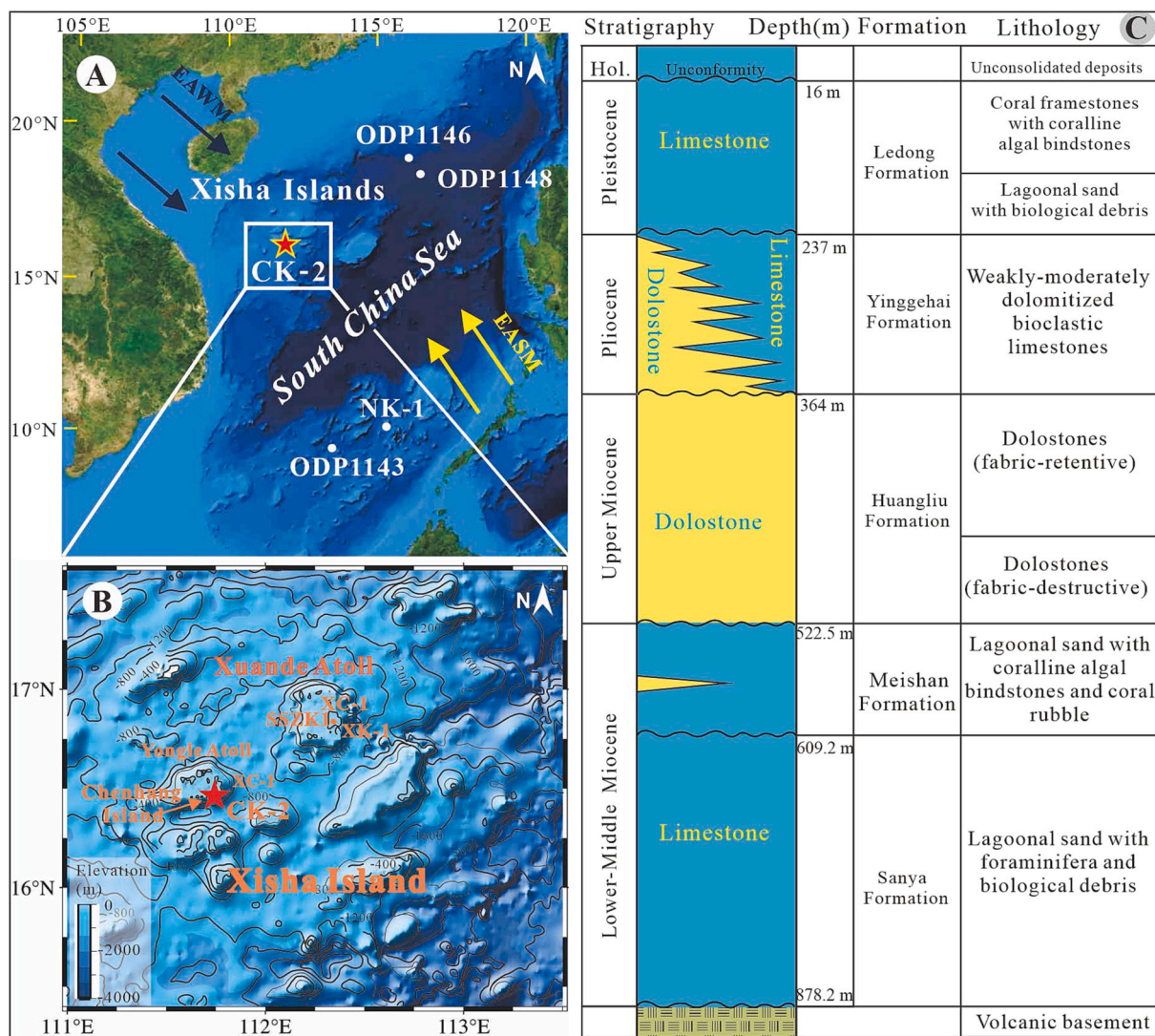

Fig. 1. (A) Location of Xisha Islands in the South China Sea (white rectangle). EASM: East Asian Summer Monsoon; EAWM: East Asian Winter Monsoon. (B) Location map of well Chenke 2 (CK-2) (red star). Note: This map is based on SRTM digital elevation model standard map [https://doi.org/10.1029/2019EA000658]. (C) Carbonate stratigraphic sequence of Xisha Islands based on well CK-2 (Wang et al., 2018). (For interpretation of the references to colour in this figure legend, the reader is referred to the web version of this article.)

2. Geological setting

The Xisha Islands (17°07′-15°43′ N, 111°11′-112°54′ E), located along the passive continental margin to slope area of the northern South China Sea, include >40 islands, banks, reefs, and shoals, with an overall land area of 8 km² (Fig. 1A) surrounded by water up to 1000 m deep (Ma et al., 2011). Today, the climate of the Xisha Islands is influenced by southwest monsoons during summer and northeast monsoons during winter (Hu et al., 2000). In the Xisha region, the annual precipitation is 1300–2000 mm/year, the average sea surface temperature (SST) is 22–30 °C, and the sea surface salinity is 33.14–34.24‰ (Shao et al., 2017a).

The carbonate successions of the Xisha platform developed on Jurassic and/or Cretaceous metamorphic/volcanic basement rocks that are ~1200 m thick (Yang et al., 2016; Zhang et al., 2020). The Xisha platform flourished in the early Middle Miocene (Wang et al., 2018; Wu et al., 2021), declined in the late Middle Miocene, was submerged in the Pliocene-Quaternary, and has since reduced in size (Zhao, 2010; Kuang et al., 2014; Shao et al., 2017a). Drill cores and seismic data show that the Xisha carbonate succession can be divided into five unconformity bound units; the Sanya Formation, Meishan Formation, Huangliu Formation, Yinggehai Formation, and Ledong Formation (Fig. 1C) (Wang et al., 2018).

Well CK-2, drilled on Chenhang Island (110°00′54″E, 16°26′56″N), Xisha Islands (Fig. 1B), is 928.75 m long with an average recovery rate of >70%. The core penetrated the pyroclastic rocks of the basement (878–928 m below sea floor, mbsf, hereafter simply referred to as m) and their thick limestone cover (0–878 m) (Fig. 1C) (Fan et al., 2020; Zhang et al., 2020). The carbonate strata of CK-2 can be divided into four

sections based on age; 0–16.7 m for the Holocene, 16.7–237 m for the Pleistocene, 237–308.5 m for the Pliocene, and 308.5–878.21 m for the Miocene (Wang et al., 2018; Fan et al., 2020). This subdivision is based on Sr isotope data (*n* = 27), paleomagnetic data (*n* = 52), and uranium series dating (*n* = 17) from Jiang et al. (2019), Qin et al. (2019), Fan et al. (2020), and Ma et al. (2021) the carbonates at ~221 m depth precipitated at ~2.37 ± 1.5 Ma (early Pleistocene) and those at ~0.6 m depth precipitated ~3933 ± 31 a (Fig. 2).

3. Materials and methods

Samples from the upper ~237 m of core CK-2 were examined in this study. The core is characterized based on composition, sedimentary textures, and sedimentary structures using 79 thin sections (3 cm*4 cm*5 cm, 30 μm thickness) prepared from coral free areas of the core at ~3 m intervals at Nanjing University. Two hundred and thirty-seven powdered samples (5–10 g) were drilled at 1 m intervals using a dental drill. These powders were then flushed and desalted, ground with an agate mortar and pestle, sieved with a 200 mesh, and dried in an electric thermostatic (40 °C) blast drying oven for 12 h. The dried powders were analyzed for their mineral compositions, carbon and oxygen isotopes ($\delta^{13}C$, $\delta^{18}O$), trace elements (Sr, Mn, Fe), and Rare Earth Elements and yttrium (REE + Y) concentrations. All analyses were performed at Guangxi Laboratory, Study of Coral Reefs in the South China Sea, China.

Twenty-six powdered samples (5–10 m intervals) were analyzed for X-ray diffraction (XRD) using an X'Pert PRO diffractometer. The analysis was conducted with the 2θ between 10°-80°, voltage of 40 kV, and current of 35 mA. Carbon and oxygen isotopic analysis of 237 powdered
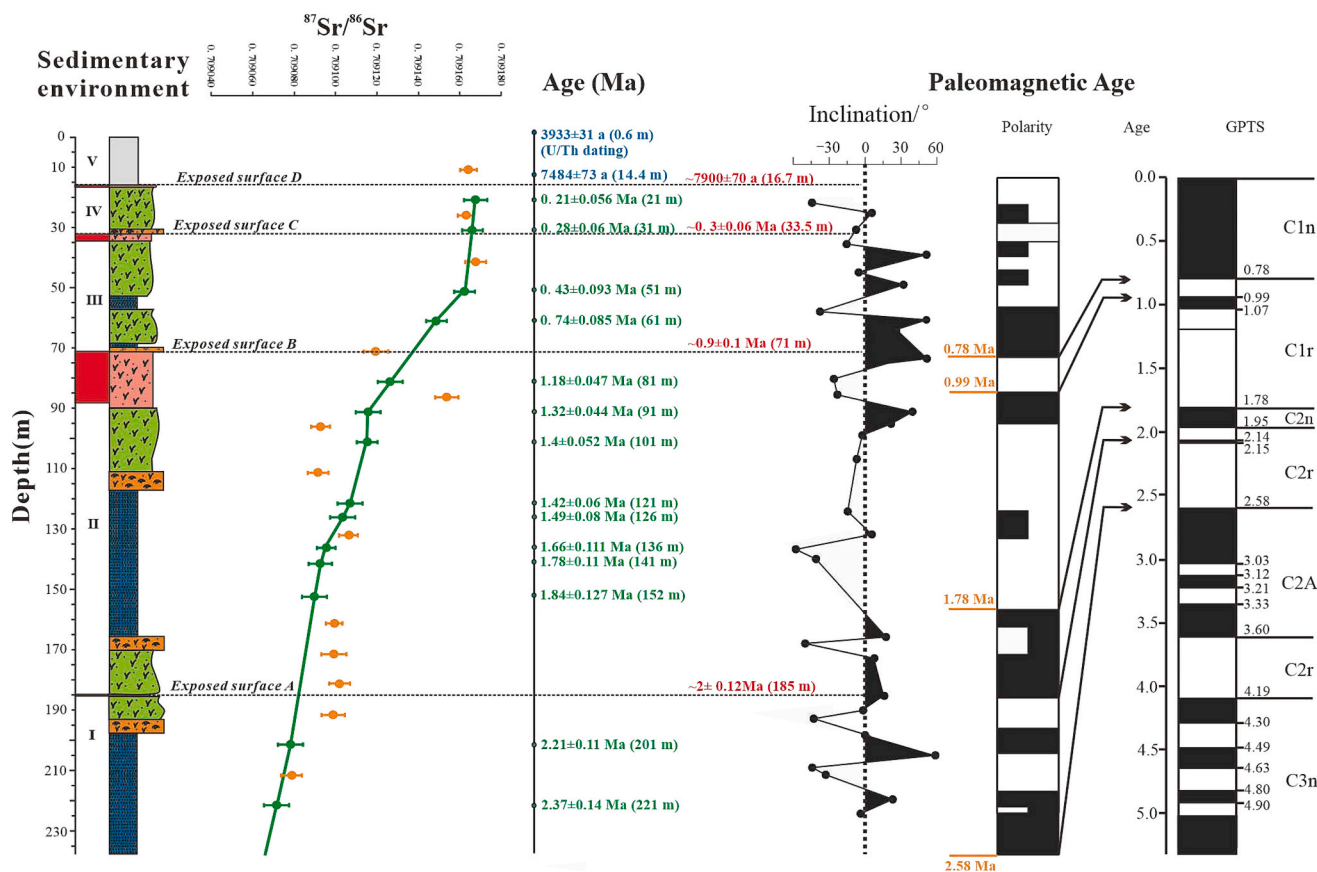

Fig. 2. Age framework of Pleistocene-Holocene succession (0–237 m) in well CK-2, Xisha Islands. Sr isotope ages from Jiang et al. (2019) (green), paleomagnetic ages from Fan et al. (2020) (orange), and U/Th dating for Holocene from Ma et al. (2021) (blue). Note: please see Fig. 3 for sedimentary environmentsand Supplementary Table 1 for detaied ages and errors. (For interpretation of the references to colour in this figure legend, the reader is referred to the web version of this article.)

samples (20 mg) were performed on a Finnigan MAT-253 stable isotope ratio-mass spectrometer. Powdered samples were placed in an automatic carbonic acid apparatus to react with 100% H_3PO_4 at 75 °C, and CO_2 was extracted after reaction. Isotope ratios were normalized to Vienna Pee Dee Belemnite (VPDB) according to the GBW04405 standard ($\delta^{13}C = 0.57‰$, $\delta^{18}O = -8.49‰$). Multiple measurements ($n = 15$) yielded standard deviations of $\pm 0.03\%$ and $\pm 0.08\%$ for $\delta^{13}C$ and $\delta^{18}O$, respectively. Although 237 samples underwent isotopic analysis, some samples were rejected due to poor data quality, therefore, 231 samples are used in this study.

Two hundred and thirty-seven powdered samples were analyzed for trace elements and REE + Y. Each sample (40 mg) was mixed with 2 ml of 1:10 HF-HNO$_3$ solution in a polytetrafluoroethylene digestion tube and heated at 180 °C for 24 h. Then 1 ml of ultrapure water and 1 ml of 2% HNO$_3$ were added to the digestion bath, which was heated again at 180 °C for 12 h. The samples were then dissolved with a 2% HNO$_3$ solution, and the volume was fixed to 80 g. Finally, the samples were analyzed by Inductively Coupled Plasma Mass Spectrometry. To monitor the accuracy and precision of the analysis, parallel samples were added between every 10th sample, and standards (GBW07129, GBW07133, GBW07135) were tested congruently. The samples were calibrated according to the standards, and the accuracies, controlled by the standard and parallel samples, yielded deviation values of <5% with a precision of one part per million (ppm). Although 237 samples were analyzed for trace elements and REE + Y, some samples were rejected due to poor data quality, therefore, 232 samples are used in this study.

4. Results

4.1. Mineralogy and petrography

The Pleistocene-Holocene carbonate succession (0–237 m) from CK-2 can be divided in five units (Units I-V) based on composition, sedimentary texture, and sedimentary structures (Fig. 3). The Pleistocene-Holocene carbonate rocks from CK-2 are formed of low-Mg calcite (LMC), high-Mg calcite (HMC), aragonite, and dolomite (Fig. 3). Unit I (185–237 m) consists of LMC and dolomite; while Units II, III, and IV (16.7–185 m) are dominated by LMC (average > 98%) with minor aragonite and HMC in the top ~10 m of Unit IV. Unit V (0–16.7 m) is dominated by aragonite (45.1%) and HMC (25.2%).

Unit I (185–237 m) is characterized by wackestone-packstones with 30–60% bioclasts, mainly rhodoliths (Fig. 4A), *Halimeda*, foraminifera, and coralline algae fragments. The upper and middle sections (185–200 m) include prismatic calcite cements with minor prismatic/blocky calcite cements (<5%), while the lower section (205–237 m) contains prismatic calcite cements and minor dolomite crystals (<14%) (Fig. 5A). The whole unit is characterized by intergranular pores/vugs, including dissolution vugs at the unit top. This unit is capped by a 0.20 m thick reddish-brown iron oxide layer.

Unit II (71–185 m) is characterized by packstone-grainstones. The grainstones (71–91 m) are composed of *Acropora* and *Porites* fragments with well-preserved structures. Although the skeletal structures are well-preserved there is evidence of dissolved pores and neomorphism of aragonite to calcite in some coral skeletons. Additionally, prismatic/blocky calcite cements are present in many of the irregular pores (Fig. 5B). The packstones (91–185 m) consist of fragments of *Porites*, *Acropora*, and *Halimeda*, with moderate amounts of moldic porosity and neomorphism. Prismatic and blocky calcite cements (Fig. 5C) are commonly observed at the bottom of this unit. This unit is capped by a 16.5 m thick reddish-brown iron oxide layer.

Unit III is divided into two sections based on lithology. The lower part of Unit III (35–71 m) is dominated by packstone-grainstones consisting of fragments of *Acropora* and *Porites*, although less common than in the upper part of this unit. Dissolved pores (Fig. 5D) with prismatic and blocky calcite cements are sporadic, and fibrous calcite cements occur in <10% of this interval. The upper part of Unit III (33.5–35 m) is

dominated by grainstone-coral rudstones consisting of coral framework and fragments. These corals include specimens of *Acropora, Porites* (including fragments up to 2 m long)*, Favia* (Fig. 4B), *Leptastrea* (Fig. 4C), and *Fungia* (Fig. 4D). Prismatic, meniscus, and blocky calcite cements occur in dissolution pores. Neomorphism (Fig. 5E) exists throughout this unit. This unit is capped by a 1.5 m thick reddish-brown iron oxide layer.

Unit IV (16.7–33.5 m) is characterized by packstone-grainstones, with a skeletal assemblage with abundant corals, including, *Porites* (Fig. 4E), *Acropora*, and *Leptastrea*. Micritization, neomorphism, and dissolved pores including moldic porosity are well developed in this unit. This unit is capped by a 0.75 m thick reddish-brown iron oxide layer.

Unit V (0–16.7 m) is characterized by unconsolidated carbonate sand and coral breccias, containing *Acropora* (Fig. 4F) and *Porites*. Some of the *Acropora* branches are covered with algae. Epitaxial acicular cements have developed on the internal pores of some coral fragments (Fig. 5F).

4.2. Elemental compositions

Elemental concentrations vary throughout well CK-2 and can be related to the age of the succession. The Fe concentration ranges from 152.4 to 2047.9 ppm (average 386.9 ppm) in Units I-V. The Pleistocene interval (16.7–237 m) records an overall decrease in values from ~500 to 100 ppm up core and a reduction in mean Fe concentration to 367 ppm. There are, however, elevated Fe concentrations (>900 ppm) in the 80–100 m and 50–60 m intervals. The Fe concentration increases significantly at the Pleistocene-Holocene interface, with the Holocene interval (0–16.7 m) being characterized by fluctuating values and a mean Fe concentration of 634 ppm (Fig. 6A).

The Mn concentration ranges from 2 to 239 ppm (average 44 ppm) in Units I-V. The Pleistocene interval records an overall decreasing trend from ~100 to 30 ppm up core. Although there is a uniform decrease in Mn content up core, from 160 –185 m and 55–90 m the Mn content fluctuates considerably. There is a significant decrease in the Mn concentration at the Pleistocene-Holocene interface, where the mean value decreases from 228 ppm in the Pleistocene samples to 44 ppm in the Holocene samples (Fig. 6B).

The Sr concentration ranges from 138 to 7521 ppm (average 1000 ppm) in Units I-V. The Pleistocene interval records an overall increasing trend from ~140 to 2500 ppm up core with a mean value of 748 ppm. There is a sharp increase in the Sr content at the Pleistocene-Holocene interface. The Holocene interval is characterized by fluctuating values from ~3000 to 7500 ppm and a mean Sr concentration of 4468 ppm (Fig. 6C). The Mn/Sr ratios from this well display values typically <0.5 with an overall decreasing trend throughout the Pleistocene and Holocene intervals, however, the Mn/Sr values from the Holocene interval are significantly lower than those from the Pleistocene (Fig. 6D).

The $\sum$REE + Y content varies from 18 to 1633 ppm (average 620 ppm) in Units I-V with an overall decreasing trend up core (Fig. 6E). The light rare earth element/heavy rare earth element (LREE/HREE) values range from 0.19 to 0.78 (average 0.33), showing an enrichment of HREE throughout the core (Fig. 6F).

4.3. Carbon and oxygen isotopes

The carbon isotope values range from −6.29 to +2.24‰ (mean = 1.05 ‰) (Fig. 6G), and the oxygen isotope values range from −8.79 to +3.02‰ (mean = −5.24 ‰, $n = 231$) throughout well CK-2 (Fig. 6H). Unit I is characterized by slightly increasing $\delta^{13}C$ values from +0.75 to +2.2‰ and slightly decreasing $\delta^{18}O$ values from +3.0 to +0.3‰. Unit II-IV are characterized by $\delta^{13}C$ values from −6.29 and + 0.75 ‰ and $\delta^{18}O$ values from −8.8 to +0.5‰. The $\delta^{13}C$ values display an overall decreasing trend throughout Unit II (71–185 m) and IV (16.7–33.5 m), whereas Unit III (33.5–71 m) displays an initial increase followed by a decreasing trend up core. The $\delta^{18}O$ values display a slight decreasing
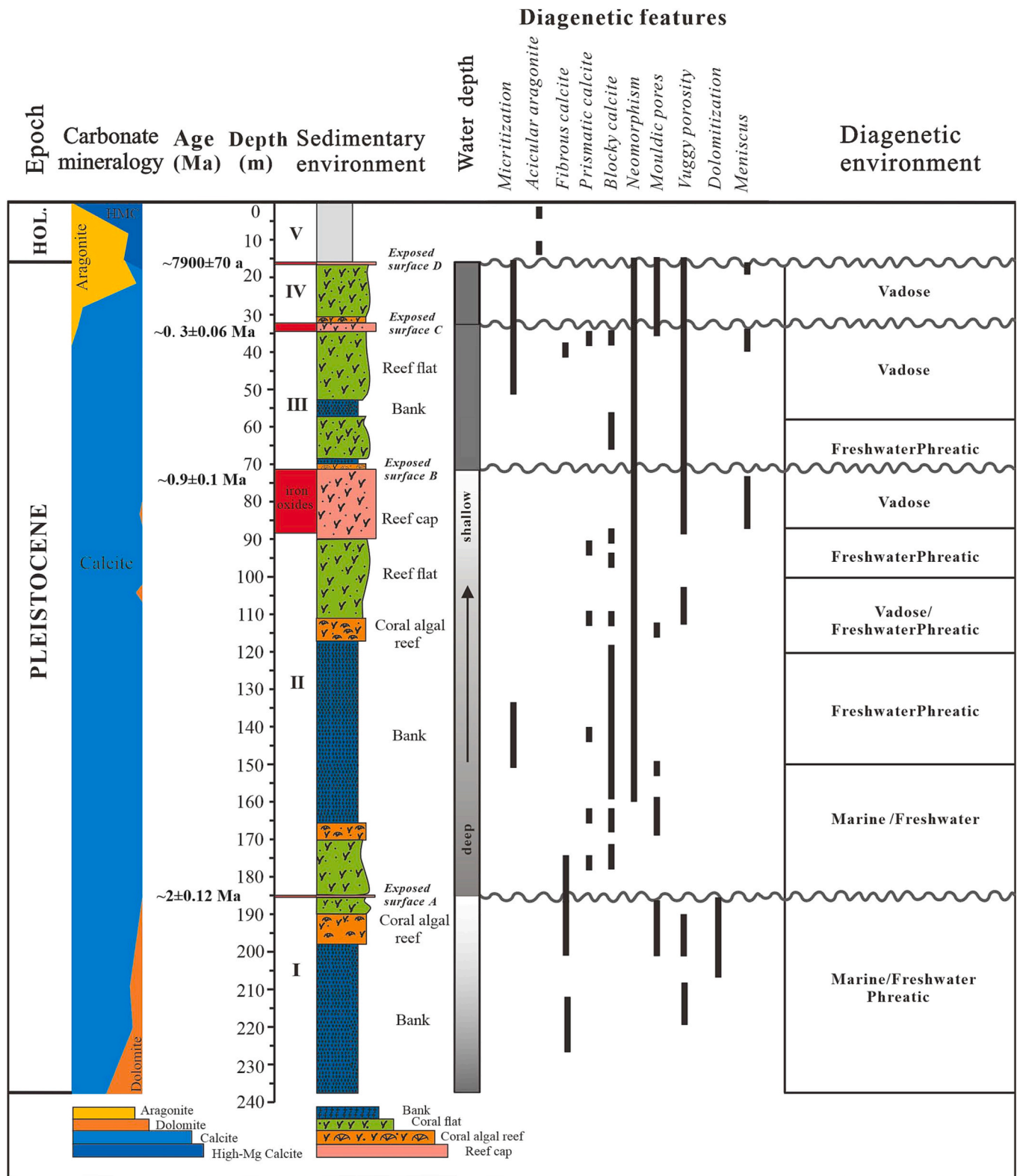
Fig. 3. Mineralogy, sedimentary environment, diagenetic features, and diagenetic environment of the Pleistocene-Holocene carbonate rocks in well CK-2, Xisha Islands. Note: wavy lines represent exposed surfaces (unconformities); capitals A to D are exposed surface identifiers; roman numerals I to V refer to the unit numbers; the red square indicates the length of iron oxides under the exposed surfaces. (For interpretation of the references to colour in this figure legend, the reader is referred to the web version of this article.)
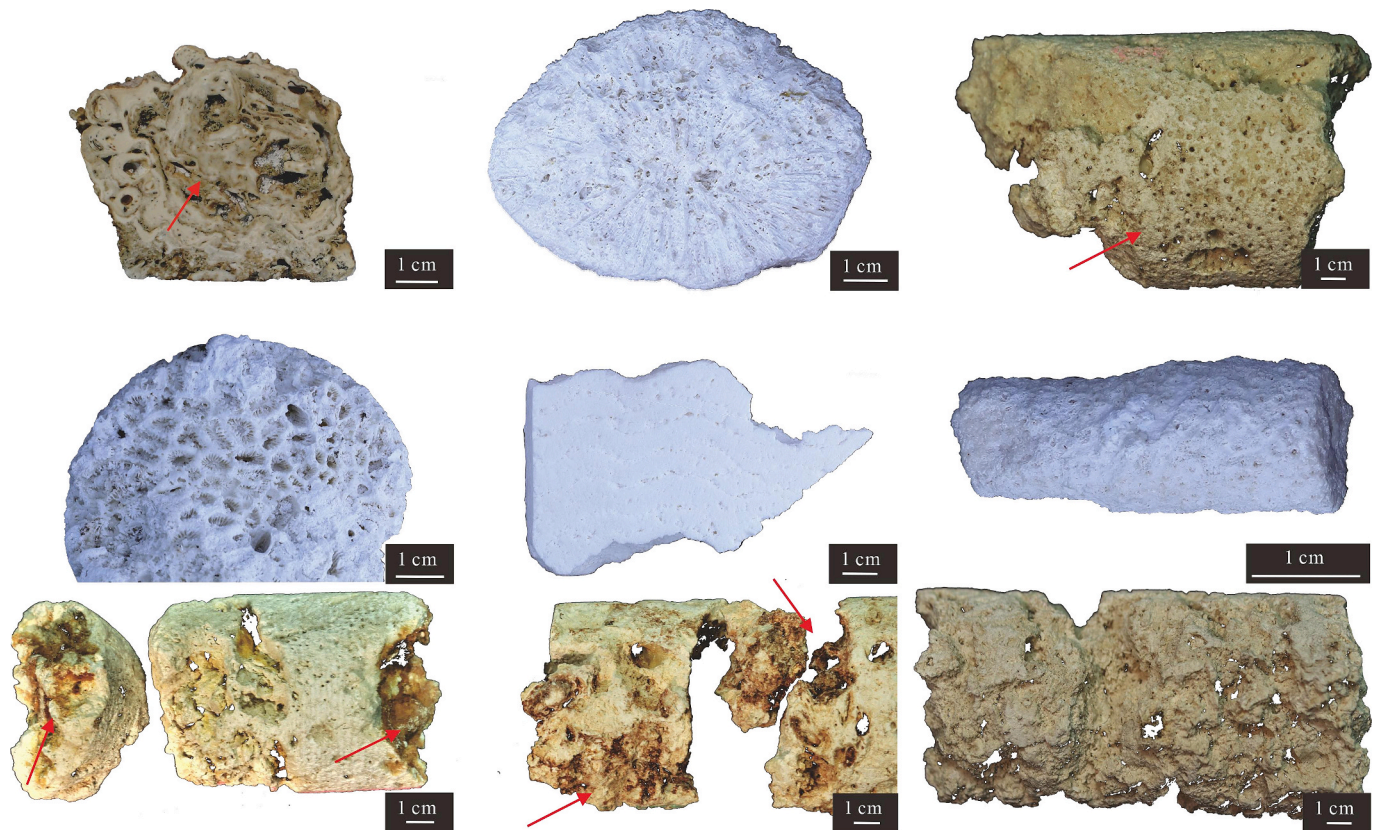
Fig. 4. Core photographs from the Pleistocene carbonate succession in well CK-2, Xisha Islands. (A) Core at 62.54 m, ~4 cm in diameter rhodoliths (red arrow). (B) Core at 63.8 m, well preserved *Favia*. (C) Core at 42.75 m, well-preserved *Leptastrea* (red arrow) with corroded surface. (D) Core at 45.2 m, well preserved *Fungia*. (E) Core at 29.6 m, well preserved *Porites*. (F) Core at 13.05 m, ~1 cm in diameter of *Acropora* coral branches with surface consolidation and indistinguishable details. (G) Obvious iron oxides (red arrow) under 77 m exposed surface. (H) Prominent iron oxides (red arrows) near the 33.5 m exposed surface. (I) Core at 33.8 m, slightly yellow surface with dissolution pits.

trend throughout Units II-IV. There is a sharp transition to higher isotopic values at the Pleistocene-Holocene transition. The Holocene interval (Unit V; 0–16.7 m) is characterized by $\delta^{13}C$ values from −3.8 to +1.8‰ and $\delta^{18}O$ values from −8.5 to −2.1‰. This transition to less negative isotopic values is associated with the major mineralogical change from LMC in Units II-IV to aragonite and HMC in Unit V. Comparing the isotope values of this core against each other highlights the presence of an inverted "J" shape (Fig. 7).

4.4. Unconformities, stratigraphic units, and age

The transition from Units I to II (interface denoted as A) is represented by an unconformity surface at 185 m, which is characterized by 1) a decrease in the amount of dolomite (Fig. 3), 2) a decrease in the Fe and Mn contents, Mn/Sr ratio, and $\sum REE + Y$, 3) a slight increase in the Sr content, 4) a rapid decrease in $\delta^{18}O$ values (mean values from +1.20‰ in Unit I to −7.2‰ in Unit II), 5) a sharp decrease in $\delta^{13}C$ values (mean value from +1.27‰ in Unit I to −2.09‰ in Unit II) (Fig. 6), and 6) a thin layer (~0.20 m thick) of iron oxides with significant dissolution pores beneath the interface. $^{87}Sr/^{86}Sr$ ratios and paleomagnetic evidence suggest that this interface may have been generated at ~2 ± 0.12 Ma (Jiang et al., 2019; Fan et al., 2020) (Fig. 2; S-Table 1).

The transition from Units II to III (interface B) is represented by an unconformity surface at 71 m, which is characterized by 1) a slight increase in Mn and Sr contents, 2) a slight decrease in Fe content and $\sum REE + Y$, 3) an increase in $\delta^{13}C$ values (Fig. 6), and 4) obvious iron oxides (~16.5 m thick) below the interface (Fig. 4G) with many vuggy pores (7–8 m thick). $^{87}Sr/^{86}Sr$ and paleomagnetic evidence suggests that the age of the exposed surface may have been generated ~0.9 ± 0.1 Ma

(Jiang et al., 2019; Fan et al., 2020) (Fig. 2; S-Table 1).

The transition from Units III to IV (interface C) is represented by an unconformity surface at 33.5 m, which is characterized by 1) a decrease in LMC and an increase in aragonite with minor HMC (Fig. 3), 2) slightly increasing Sr values, 3) a decrease in $\delta^{13}C$ values (mean value from −1.13‰ in Unit III to −2.11‰ in Unit IV) (Fig. 6), and 4) obvious iron oxides (1.5 m thick) beneath the interface with vuggy pores (Fig. 4H, I). $^{87}Sr/^{86}Sr$ and paleomagnetic evidence suggests that the age of the exposed surface may have been generated ~0.3 ± 0.06 Ma (Jiang et al., 2019; Fan et al., 2020; Yang et al., 2022) (Fig. 2; S-Table 1).

The transition from the Pleistocene to the Holocene successions (interface D) is represented by an unconformity surface at 16.7 m, Uranium series dating and linear extrapolation suggests that the age of the exposed surface may have been generated ~7900 ± 70 years ago (Qin et al., 2019; Ma et al., 2021) (Fig. 2; S-Table 1). This surface is characterized by 1) a complete loss of LMC and an increase in HMC and aragonite (Fig. 3), 2) elevated Fe and Sr concentrations, 3) decreasing Mn/Sr ratios, 4) an increase in the $\delta^{13}C$ and $\delta^{18}O$ values (mean values from −1.90‰ in Unit IV to −0.12‰ in Unit V and mean values from −7.9‰ in Unit IV to −3.94‰ in Unit V, respectively) (Fig. 6), and 4) obvious iron oxides (0.75 m thick) beneath the interface.

4.5. Stratigraphic age evaluation

All the dates used in this study were taken from previous research on well CK-2 and the dated material corresponded to well-preserved sediments and corals. The current study combined the numerous ages produced from well-preserved materials in core CK-2, including Sr isotope stratigraphy, U/Th dating, and magnetostratigraphy with linear
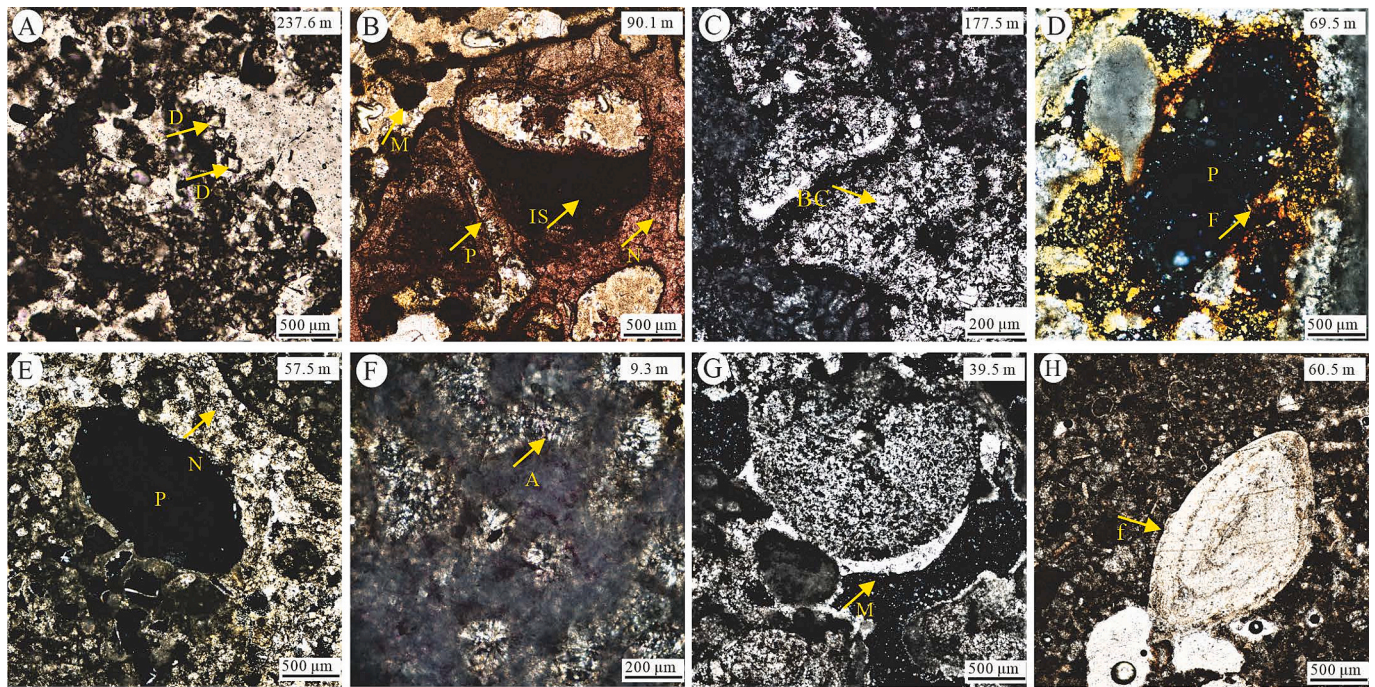
Fig. 5. Characteristic diagenetic features in thin sections of Pleistocene-Holocene rocks from CK-2, Xisha Islands. Depths specified in upper right corner of each image are below present-day sea-level. All images were taken under cross-polarized light with the exception of B that is in plane-polarized light. (A) Clear dolomite crystal (D) floating in calcite matrix. (B) Internal Sediment (IS), Micritization (M'), Prismatic Calcite (PC), and Neomorphism (N). (C) Blocky Calcite (BC) cement in pores. (D) Fe-oxides (F) coating the pore (P). (E) Neomorphism (N) to form sparry calcite. (F) Acicular aragonite (A) cement in pores of coral framework. (G) Meniscus cement (M) under a biological fragment. (H) Well preserved foraminifera (f; *Amphistegina*) in matrix.

extrapolation models to develop a robust and relatively reliable stratigraphic framework for this succession (S-Table 1) (Jiang et al., 2019; Qin et al., 2019; Fan et al., 2020; Ma et al., 2021; Yang et al., 2022). Here, the methods and criteria used to determine the degree of diagenetic alteration on the bulk carbonates include Mn/Sr ratios and $\delta^{18}O$ values (Brand and Veizer, 1980; Derry et al., 1992; Azmy et al., 2009). Various studies have suggested that carbonates with Mn/Sr ratios that do not exceed an upper limit of 2–3 indicate little or no late diagenesis and can, therefore, offer reliable Sr isotopic values (Derry et al., 1992; Kaufman et al., 1993; Kaufman et al., 1993; Dehler et al., 2005). The relatively small Mn/Sr ratios (0.001–0.487) of the Pleistocene-Holocene succession of CK-2 (Fig. 6D) suggests that the Sr concentration of the original well-preserved sediments and their Sr isotopes can be reliably used for dating. This suggests that the $^{87}Sr/^{86}Sr$ signatures used for age determination can provide reliable dating information. Additionally, it has been suggested that carbonate $\delta^{18}O$ values between −10‰ to −5‰ represent a mild degree of alteration but the effects are generally considered to be negligible, values below −10‰, however, are considered to be significantly altered (Derry et al., 1994; Kaufman and Knoll, 1995). The $\delta^{18}O$ values from well CK-2 range from −8.79 to +3.02‰, with an average of −5.24‰, values that are well within the acceptable range for interpretation. Comparing the $\delta^{18}O$ and $\delta^{13}C$ values from CK-2 results in an inverted "J" shape (Fig. 7) commonly associated with the degree of diagenetic openness in a system (Bishop et al., 2014), which indicates moderate diagenetic alteration has affected the majority of CK-2. The carbonate sediments from the Pleistocene-Holocene succession of well CK-2 have experienced mild diagenesis based on the above criteria for determining the degree of diagenetic alteration. Similar conclusions have been reached by other researchers, who suggested that these carbonates provide a robust indicator of past seawater chemistry (Fan et al., 2020; Yang et al., 2022). Therefore, given the mild degree of alteration recorded in most of core CK-2 and the combination of various dating techniques (e.g., Jiang et al., 2019; Fan et al., 2020; Ma et al., 2021), the ages used in this research provide a reasonable stratigraphic framework

for the investigated succession of well CK-2.

5. Interpretation of petrological and geochemical parameters

5.1. Meteoric diagenetic characteristics as indicated by petrology

The Pleistocene succession (16.7–237 m) from well CK-2 on the Xisha Islands consists of abundant corals (e.g., *Acropora, Porites, Favia*), coralline algae, foraminifera, and *Halimeda*. Allochems akin to the modern biota found in Xisha coral reef areas, suggesting that there was a comparable depositional environment during the Pleistocene. Similarly, based on lithological and biological components of Pleistocene cores drilled from wells XK-1 and SSZK1 on the Xisha Islands (Fig. 1A), Zhu et al. (2015) and Chen et al. (2020) suggested that these carbonate sediments originated in a shallow water reef environment (<40 m water depth). Although the sediments accumulated in shallow water, the presence of successive unconformities at the interfaces between these units suggests that these rocks were subjected to periods of subaerial exposure. These interface surfaces contain iron oxides, vuggy porosity, and abundant cementation; features similar to other subaerial exposure surfaces from carbonate platforms that have undergone meteoric diagenesis like those developed in well NK-1 in the Nansha Islands (Fig. 1A) (Luo et al., 2022) and other isolated carbonate platforms in the Pacific Ocean and Caribbean Sea (e.g., Jones, 2016; Luo et al., 2022). The suggested timing of the four exposure surfaces from CK-2 is consistent with regional (Shao et al., 2017b; Luo et al., 2022) and global sea-level drops (Haq et al., 1988; Berends et al., 2021) (Fig. 8), suggesting that the four unconformities were formed during periods of sea-level fluctuation.

The Pleistocene carbonate succession of CK-2 has undergone neomorphism, calcite cementation (meniscus, fibrous, prismatic, and blocky), and dissolution (Fig. 5); diagenetic features that are associated with meteoric diagenesis. The neomorphism is typically present from 20 to 160 m and is responsible for obscuring original coral structures and
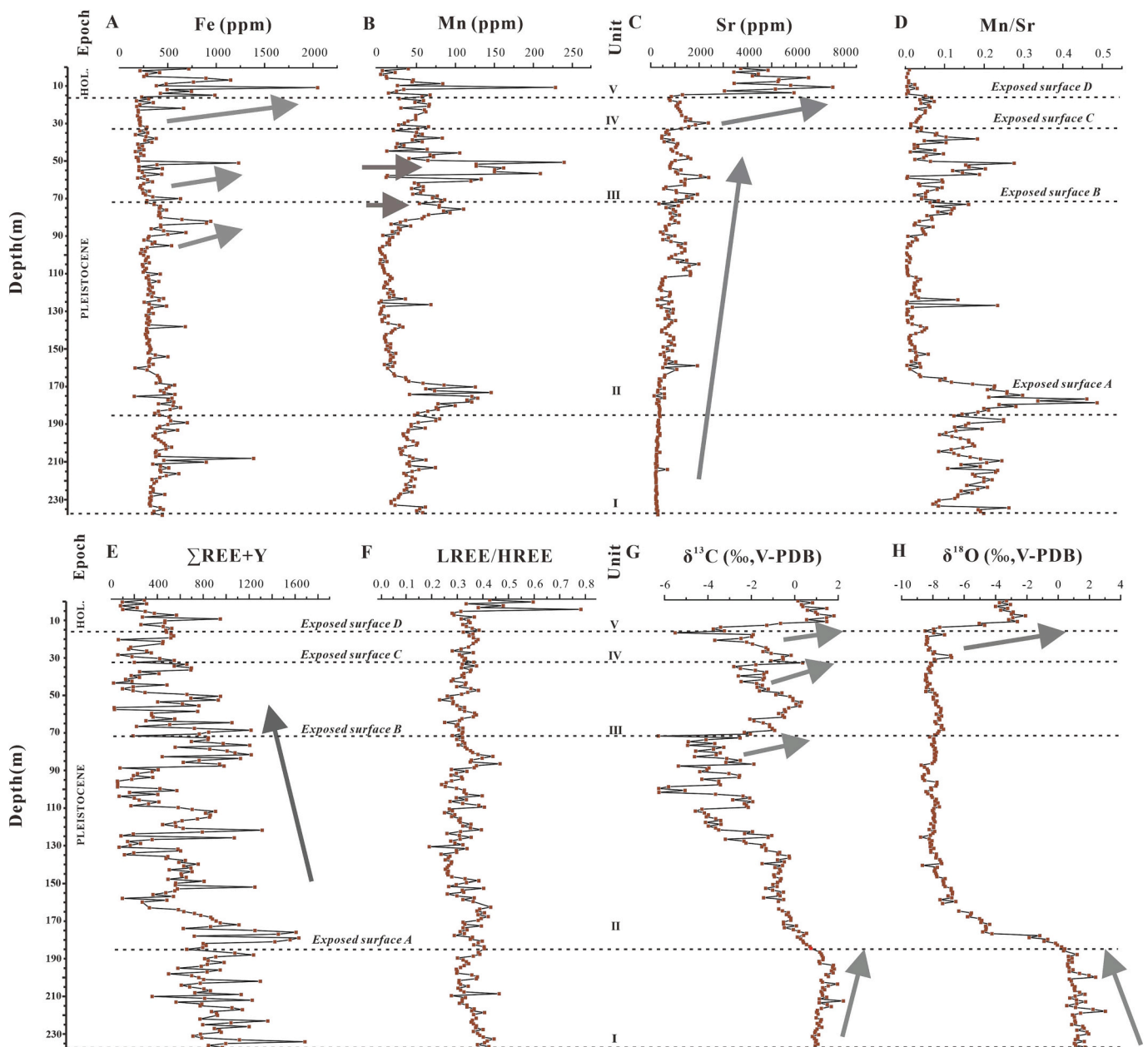
Fig. 6. Vertical variation of geochemical data from the Pleistocene-Holocene succession (0–237 m) in CK-2, Xisha Islands. Black dotted line represents the exposure surfaces and the gray arrow represents the trend of the different indexes. (A) Fe content. (B) Mn content. (C) Sr content. (D) Mn/Sr ratio. (E) $\sum$REE + Y content. (F) LREE/HREE ratios. (G) δ^{13}C values. (H) δ^{18}O values.

enlarging grains in the micritic matrix (Fig. 5E). Neomorphism has been identified in many Quaternary coral reef sediments such as the Great Barrier Reef, Australia, the southern edge of the Red Sea, Saudi Arabia, and Huon Peninsula, New Guinea (Martin et al., 1986; McGregor and Gagan, 2003), and is generally believed to be associated with fluid exchange from the intrusion of meteoric waters. Meniscus cements, common in CK-2 below the exposed surfaces (Fig. 5H), are features considered to have formed by gravity driven precipitation (Braithwaite and Montaggioni, 2009; Swart and Oehlert, 2018) in the meteoric vadose zone. Blocky calcite cements, common in CK-2, are associated with the meteoric phreatic zone, similar to those described in Holocene oolitic limestones of the Bahamas (Halley and Harris, 1979; Budd, 1988). Additionally, indiscriminate dissolution (Fig. 5D) and vuggy pores, generally developed beneath the exposure surfaces in CK-2 (Fig. 3), are probably related to non-selective dissolution by meteoric waters, like those observed in Enewetak Atoll (Saller and Moore, 1989).

Overall, the widespread development of neomorphism, meniscus and blocky cements, and numerous non-selective dissolution cavities indicates that the exposure surfaces in the Pleistocene rocks of CK-2 were altered by meteoric diagenesis.

5.2. Meteoric diagenetic characteristics as indicated by geochemical parameters

5.2.1. Carbon isotope trends

Carbon isotopes of carbonate rocks are primarily controlled by the original carbonate sediment type and diagenesis (Allan and Matthews, 1982). The δ^{13}C values (−6.29 to +0.75‰) of the Pleistocene succession in CK-2 are typically lower than those from modern shallow marine sediments (0 to +5‰) (Allan and Matthews, 1982; Swart, 2015) (Fig. 7), indicating that diagenesis has taken place. Similar negative δ^{13}C values in Pleistocene strata from wells XC-1 (δ^{13}C: −6.34 to +0.4‰) and NK-1
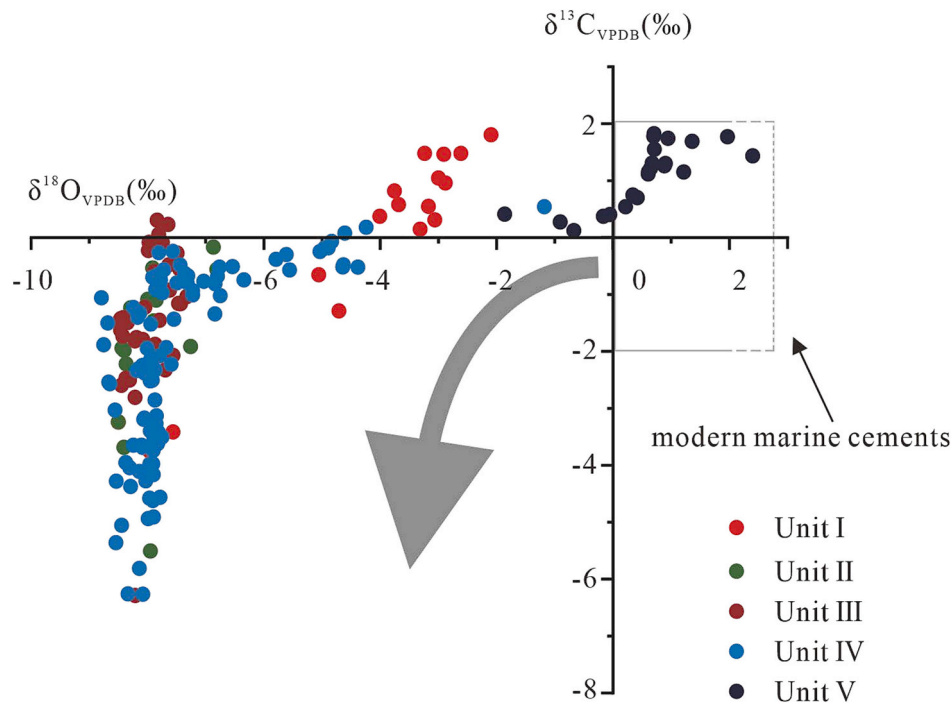
Fig. 7. Cross-plots of $\delta^{18}O$ and $\delta^{13}C$ from the different units (I to V) in the Pleistocene-Holocene succession of well CK-2 in Xisha Islands. Gray arrow indicates the variation of $\delta^{18}O$ and $\delta^{13}C$ values representing the inverted "J" shape. Note: the gray box (black arrow) represents the approximate $\delta^{18}O$ and $\delta^{13}C$ ranges of modern marine sediments (Swart, 2015). (For interpretation of the references to colour in this figure legend, the reader is referred to the web version of this article.)

($\delta^{13}C$: −8.7 to +0.3‰) in the Xisha Islands (You et al., 2015; Luo et al., 2022) have been attributed to the influence of meteoric waters. The $\delta^{13}C$ values in Units II-IV from CK-2 display a decreasing trend towards the tops of each unit with minimum values occurring below the exposed surfaces (Fig. 6G). The Pleistocene strata from XC-1 and SSZK1 (Qiao et al., 2015; Chen et al., 2020) display a similar cyclical pattern in their $\delta^{13}C$ values (Fig. 9). These negative signatures and the overall decreasing trends in the $\delta^{13}C$ values may be related to carbonate recrystallization and cementation in the vadose zone where light carbon isotopes (^{12}C) are sourced from overlying air and soil (Allan and Matthews, 1982). During sea-level lows carbonate platforms can become exposed, which facilitates the infiltration of meteoric waters in the carbonate sediments; this water will eventually reach a depth where it is no longer in contact with the air-soil gas ^{12}C reservoir. This will cause the $\delta^{13}C$ value of the fluids to rise, which will, in turn, enrich the $\delta^{13}C$ of altered limestones and secondary calcite (Emiliani, 1970; Allan and Matthews, 1977; Swart and Oehlert, 2018), causing the decreasing trends displayed by the $\delta^{13}C$ values in CK-2 below the unconformity surfaces. The cycle will then repeat based on fluctuating sea-levels. Xu et al. (2019), however, argued that since 2.3 Ma, the $\delta^{13}C$ values of original Pleistocene carbonate rocks in the Xisha area have gradually decreased due to continuous strengthening of the EAWM and a decrease in dissolved inorganic carbon in seawater. Hence, the $\delta^{13}C$ signals of the Pleistocene succession in CK-2 could represent the joint effect of primary carbonate deposition and meteoric diagenesis associated with the EAM.

5.2.2. Oxygen isotope trends

The $\delta^{18}O$ values of the Pleistocene carbonates from CK-2 between 16.7 and 140 m are generally ~ − 8.0‰ (Fig. 6H), values that are significantly lower than the $\delta^{18}O$ values of modern limestones precipitated from normal seawater (−2 to +2‰) (Saller and Moore, 1989). These $\delta^{18}O$ values, however, are similar to the $\delta^{18}O$ values of Pleistocene carbonates from wells XY-1, XY-2, XC-1, and SSZK1 ($\delta^{18}O = −8$‰) on the Xisha Islands (Zhao, 2010; You et al., 2015; Wu et al., 2019; Chen et al., 2020) (Fig. 9). These values are also similar to those of other Pleistocene carbonate sediments that have undergone meteoric

diagenesis such as the Great Barrier Reef Beach, Australia ($\delta^{18}O = −6$‰) (Braithwaite and Montaggioni, 2009), Enewetak Atoll ($\delta^{18}O = −7$‰) (Saller and Moore, 1989), the Great Bahama Bank ($\delta^{18}O = −6$‰) (Swart and Oehlert, 2018), and Barbados ($\delta^{18}O = −4$‰) (Allan and Matthews, 1982). This suggests that the original $\delta^{18}O$ values of the Pleistocene sediments from CK-2 have been similarly affected by meteoric waters. Minor discrepancies between the $\delta^{18}O$ values from the carbonates in Xisha Islands and other Pleistocene carbonate sediments may be related to the variability in local rainfall (Swart, 2015).

5.2.3. Elemental compositions

In the Pleistocene succession of CK-2, the Fe and Mn concentrations generally increase with depth (Fe: ~100 to 500 ppm; Mn: ~30 to 100 ppm) (Fig. 6A, B). Meteoric waters have been shown to contain high concentrations of Mn and Fe (500 and 50 times higher than seawater, respectively) (Brand and Veizer, 1980; Rao, 1991), which can be transferred to marine carbonates during meteoric diagenesis. Below exposure surfaces B and C in CK-2, the concentrations of Fe and Mn are high (Fe up to 940 ppm; Mn up to 209 ppm; Fig. 6A, B), which suggests alteration of the carbonate rocks by meteoric water. The Fe enrichment near the exposed surfaces (corresponding to the development of iron oxides) in CK-2 is consistent with observations of Miocene-Pleistocene laterites developed on the Cayman Islands (Jones, 2016), and suggests that the formation of reddish-brown iron oxides is related to leaching by meteoric waters. Mn/Sr ratios are often used to indicate the degree of diagenetic modifications of carbonate rocks since marine carbonates generally show an increase in Mn and a decrease in Sr content during diagenesis (Kaufman and Knoll, 1995). The relatively small Mn/Sr ratios of CK-2 (Fig. 6D) indicates that the Sr concentration of the original sediments was preserved but the Mn content may have increased due to meteoric alteration. This suggests that meteoric diagenesis occurred in a relatively closed to semi-closed (low water/rock ratio) diagenetic system relative to the two elements (Brand and Veizer, 1980; Banner, 1995). Although some researchers have suggested that REE may be affected by meteoric diagenesis (Chen and Wang, 1996; Della Porta et al., 2015) leading to a slight enrichment in HREE (Azmy et al., 2011;
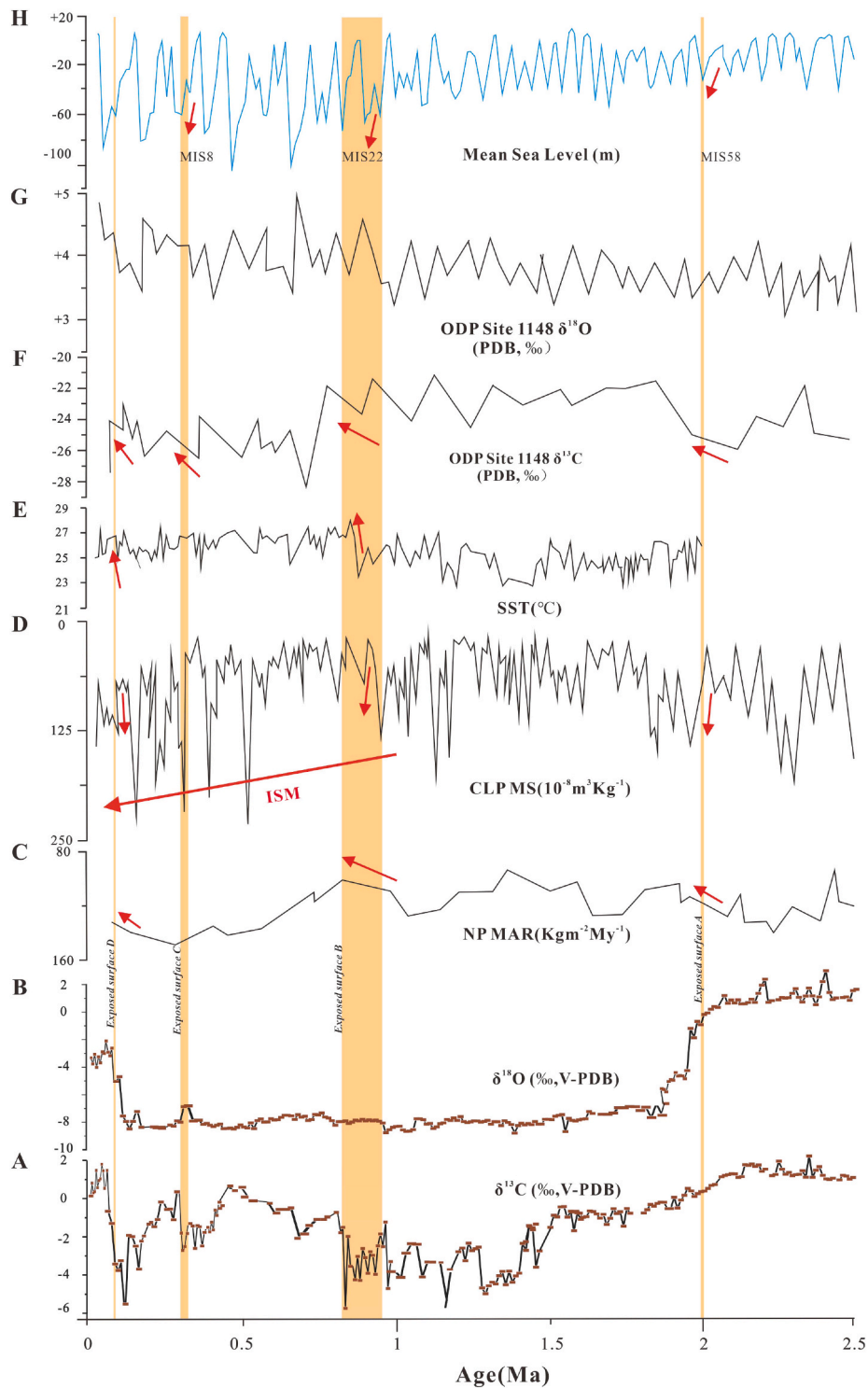
Fig. 8. Comparison of paleoclimatic/paleoenvironmental indexes from Pleistocene studies. The orange shaded areas represent the exposure surfaces in well CK-2, and the red arrows indicate trends.(A) $\delta^{13}C$ values (B) $\delta^{18}O$ values (C) North Pacific (NP) dust mass accumulation rate (MAR) (Rea et al., 1998). (D) Magnetic susceptibility recorded on the Chinese Loess Plateau (CLP) (Song et al., 2001; Guo et al., 2002; Jiang et al., 2018). (E) Sea surface temperature (SST) estimated by $\delta^{18}O$ of benthic and planktonic foraminifera at site ODP1143 (location in Fig. 1A) (Li et al., 2004). (F) Black carbon $\delta^{13}C$ at ODP1148 (location in Fig. 1A) (Jia et al., 2003). (G) Foraminifera $\delta^{18}O$ at ODP1148 (location in Fig. 1A) (Cheng et al., 2004). (H) Global sea-level change curve derived from benthic foraminifera oxygen isotopes (Berends et al., 2021). Note: The points with accurate age values for the corresponding depth of $\delta^{13}C$, $\delta^{18}O$ are presented accurately in the figure, and the presentation of other sites assumes the same depositional rate. ISM: intensified summer monsoon.

Webb et al., 2009), many studies believe that REE are conservative during meteoric diagenesis and should reflect the original depositional conditions (Kamber and Webb, 2000; Webb et al., 2009; Siahi et al., 2018; Luo et al., 2021). In the carbonate sediments from CK-2, the original REE concentrations seem to be preserved given the general consistency in the LREE/HREE values. The $\sum REE + Y$ displays a large scale gradual decrease throughout the core with smaller scale cyclical decreasing trends in each unit with minimum values associated with the
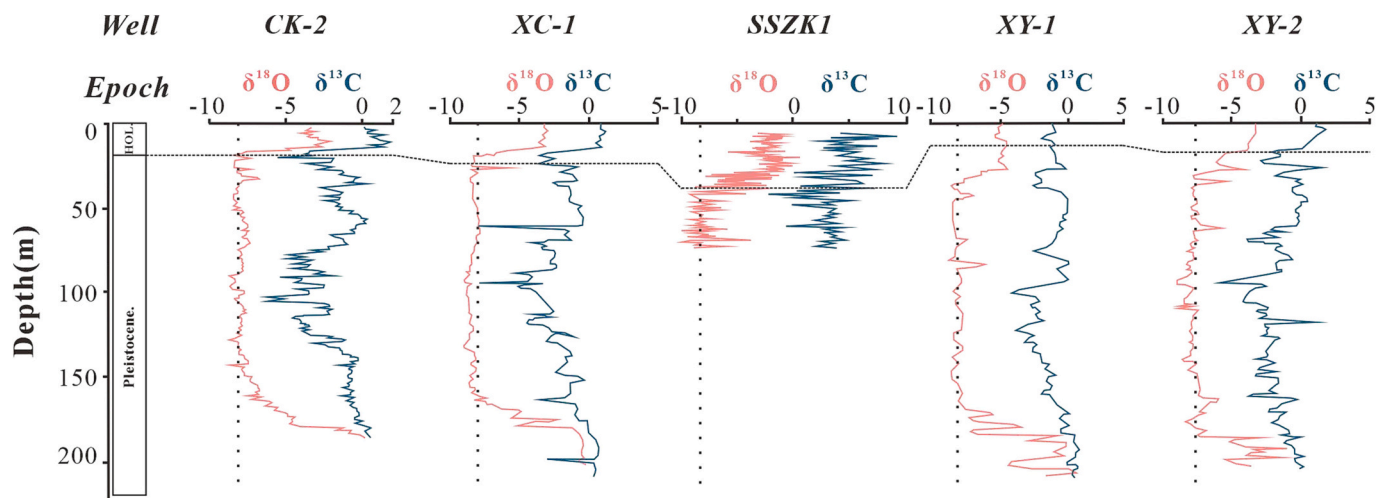
Fig. 9. The δ^{18}O and δ^{13}C of wells from the Xisha Islands, the vertical dashed line is −8.0‰ the average δ^{18}O value from the Pleistocene-Holocene succession in well CK-2 (CK-2:111°00′54″ E，16°26′56″ N；XC-1:112°25′24″ E，16°25′24″ N；SSZK1:112°18′ E，16°8′ N；XY-1:112°20′ E，16°50′ N；XY-2:112°20′ E；16°51′ N) (Zhao, 2010; Shao et al., 2017a; Chen et al., 2020).

exposed surfaces (Fig. 6E). The large scale gradual decrease in∑REE + Y throughout the core may reflect a drier climate with an associated decreased supply of terrigenous materials (∑REE + Y) due to an enhanced EAWM during the Pleistocene (Jiang et al., 2019). The isotopic, elemental, petrological, and mineralogical data from the Pleistocene carbonates of CK-2 highlight the effects of meteoric diagenesis and provide hints of paleoclimatic changes associated with precipitation related to the EAM.

6. Discussion

The petrologic and geochemical characteristics of well CK-2 indicate that the Pleistocene succession was profoundly influenced by meteoric alteration during low sea-level. During this period of low sea-level the platform was exposed to meteoric waters whose characteristics were controlled by temperature and precipitation associated with the EAM (cf., André and Strohmenger, 2010; Li and Jones, 2013; Al-Ramadan, 2021). Although there is evidence that a strengthened EAWM has influenced the northern part of South China Sea since ~4 Ma (e.g., Wan et al., 2007; Clift et al., 2014), the majority of the current rainfall in the Xisha Islands is related to the relative intensity of EASM (Liu et al., 2007), therefore, several geochemical proxies of limestone alteration (δ^{13}C, iron oxide layers, Fe, Mn, REE + Y, cements, mineral composition) influenced by rainfall were identified in the Pleistocene section of well CK-2. Specifically, the thickness of the iron oxide layers, decreases in δ^{13}C values, and increases in Fe, Mn, and REE + Y below the unconformity surfaces in the Pleistocene strata, all which indicate wet conditions during periods of subaerial exposure.

With regards to the carbon isotopic signal, the longer the carbonate sediments are exposed to meteoric diagenesis the more negative the δ^{13}C values of the platform carbonates become (cf., Swart and Oehlert, 2018). This is related to the development of vegetation, which can profoundly affect the ^{12}C content of groundwater in regions with abundant rainfall and/or warm-humid conditions (Huang, 2010). Some studies have suggested that soil gas in humid areas is more ^{12}C-enriched than in arid areas, which may lead to an increase in ^{12}C moving through the sediments of humid climates (Rightmire and Hanshaw, 1973). Enhanced EASM, which is associated with elevated temperatures and abundant rainfall, would increase the overlying vegetation on a carbonate platform and indirectly increase the ^{12}C values of the soil gas (Rightmire and Hanshaw, 1973; Huang, 2010). Meteoric water that percolates into the platform would be ^{12}C-rich, resulting in depleted δ^{13}C values in the exposed platform deposits (Christl et al., 2012), similar to the patterns

observed in the exposure surfaces in CK-2 (Fig. 6G). Additionally, the δ^{13}C curve of the Pleistocene secession in CK-2 displays an overall decreasing trend up core (Fig. 6G), which may be associated with a strengthening of the EASM and an associated increase in precipitation affecting this area.

It is clear from the elemental data that the exposure surfaces of well CK-2 underwent significant weathering and leaching. Elements such as Fe, for example, were not removed from the system, but instead concentrated to form calcareous laterites, the thickness of which is probably related to the volume of rainfall, as is the case on the Cayman Islands (Jones, 2016). Climatic change is also recorded by the REE + Y data, which shows a significant increase in ∑REE + Y near the exposure surfaces (Fig. 6E). Jiang et al. (2019) suggested that increasing ∑REE + Y content near exposed surfaces could be related to enhanced EASM, because increased precipitation caused by climatic warming would lead to an intensification of continental weathering, which in turn increases the REE + Y input to the ocean. The extensive dissolution under the exposed surfaces is also consistent with the influence of meteoric weathering, likely due to increased rainfall associated with an enhanced EASM.

Examination of the Pleistocene units individually can provide insights to the climate dynamics operating during this time. The exposure surface B at the top of Unit II (~0.9 ± 0.1 Ma) in CK-2, for example, is an ideal candidate for studying increased rainfall associated with a strong EASM. This unit displays the thickest iron oxide layer (16.5 m), the most negative δ^{13}C values (−6.2‰), and high Fe, Mn, and ∑REE + Y concentrations beneath the exposed surface. Several studies have proposed a period of increased rainfall and a strong EASM around this time of the Pleistocene in this region (e.g., Gai et al., 2020; Sun et al., 2022). Loess and soil moisture from mainland China recorded a significant increase in the intensity of EASM during the Mid-Pleistocene climate transition (~1.0–0.9 Ma) (Fig. 8. C, D) (Ding et al., 1994; Liu et al., 1998b; Gai et al., 2020; Sun et al., 2022). Additionally, deep marine sediment cores ODP1143 and ODP1146 in the South China Sea (Fig. 1A) recorded a SST increase (~1 °C) from ~1.2–0.9 Ma (Li et al., 2004; Lu et al., 2021) (Fig. 8E). The paleoclimatic conditions evidenced by the loess and the deep marine sediments (Fig. 8 F, G) are consistent with the petrographic and geochemical data from exposure surface B in Unit II.

Differences between the diagenetic features of exposure surfaces A (~2 ± 0.12 Ma), C (~0.3 ± 0.06 Ma), and D (~7900 ± 70 a) from exposure surface B suggests that the relative intensity of the EASM was changing throughout the Pleistocene and Holocene. Based on the petrographic and geochemical evidence from these exposure surfaces it

can be suggested that the EASM was weakened at ~2.5–1.0 Ma (when exposure surface A may have developed) and was strengthened from ~1.0 Ma onward (when exposure surfaces B—D may have developed) (Fig. D) (cf., Wan, 2006). The meteoric diagenetic features (LMC only and thin iron oxide layer) and relatively low $\sum$REE + Y concentrations associated with exposure surface A may indicate that the EAWM was dominant in this period, which is consistent with the results from ODP1143 (Li et al., 2004) (Fig. 8E). The negative δ^{13}C values and the 1.5 m thick iron oxide layer below exposure surface C (~0.3 ± 0.06 Ma), however, indicates enhanced rainfall, which is consistent with the findings from the planktonic foraminiferal δ^{13}C curve at ODP1148 (Fig. 8F), suggesting an enhanced EASM at this time (cf., Jian et al., 2003). The magnitude of the EASM during the development of exposure surface C, however, was likely weaker than during the development of exposure surface B, due to the slightly negative δ^{13}C values and the presence of aragonite beneath exposure surface C. Exposure surface D (~7900 ± 70 a) at the Pleistocene/Holocene interface contains abundant aragonite and HMC (Fig. 3) and the lowest $\sum$REE + Y concentrations in this record, which may suggest a generally arid climate. These findings are consistent with Huang et al. (1997) and Li et al. (2018) based on a decreased SST (2–3 °C) around Xisha Islands at this time. Additionally, Harrison (1975) showed that in humid regions HMC is completely lost in <83,000 years and aragonite in <200,000 years, whereas in the arid region of Barbados both aragonite and HMC have been identified in sediments up to 300,000 years old (Matthews, 1968). This suggests that the minor meteoric diagenesis associated with exposure surface C and D may have been partially facilitated by the intensity of the EASM. Although the paleoclimate during Pleistocene glacial periods (associated with low sea-level) (Fig. 8H) was cool and dry in various locations globally (e.g., Damuth and Fairbridge, 1970; Bonatti and Gartner, 1973), the Pleistocene carbonates of CK-2 on the Xisha Islands suggest the exposed strata were affected by wet and warm conditions due to changes in the relative intensity of EASM (Fig. 10).

The Quaternary experienced fluctuating climate states that lead to many glacial-interglacial cycles that were associated with rapid sea-level change worldwide, as such exposed carbonate sediments/rocks would have been affected by meteoric diagenesis (e.g., Braithwaite and Camoin, 2011; Ren and Jones, 2016; Swart and Oehlert, 2018). Some studies have suggested that during sea-level change, older stratigraphic intervals would have transitioned into and out of various hydrologic zones, leading to repeated and pervasive diagenetic overprinting (Matthews and Frohlich, 1987; Whitaker, 1997). Recently, however, it has been shown that successive overprinting due to sea-level change may not be identifiable in carbonate platforms (e.g., Braithwaite and Camoin, 2011; Ren and Jones, 2016; Swart and Oehlert, 2018). Instead, during sea-level lows, the diagenesis may reflect the distribution of the ground water zone during specific emergence events because the precursor metastable minerals (aragonite and HMC) would have transitioned to a more stable mineral (LMC) when first exposed (Braithwaite and Camoin, 2011; Ren and Jones, 2016; Swart and Oehlert, 2018). This scenario is the most likely case for the Pleistocene succession of well CK-2 due to the types of calcite cement observed in this core (Fig. 5). The geochemical data from the Pleistocene section of CK-2, therefore, records the climate variability (intensity of the EASM) associated with the first exposure of these carbonate sediments/rocks. Hence, the relationship between EASM intensity and meteoric diagenesis during the Pleistocene and Holocene on the Xisha Islands can provide insights about diagenesis on other carbonate platforms in monsoon regions.

7. Conclusions

Petrologic and geochemical data from the Holocene and Pleistocene carbonates on the Xisha platform indicate that deposition and meteoric diagenesis were influenced by the East Asian Monsoon. During the Pleistocene, the climate became arid due to enhanced East Asian Winter Monsoon, which resulted in the development of four distinct exposed surfaces on the Xisha platform due to sea-level fluctuations. During low sea-level, when the Pleistocene carbonates were exposed, meteoric
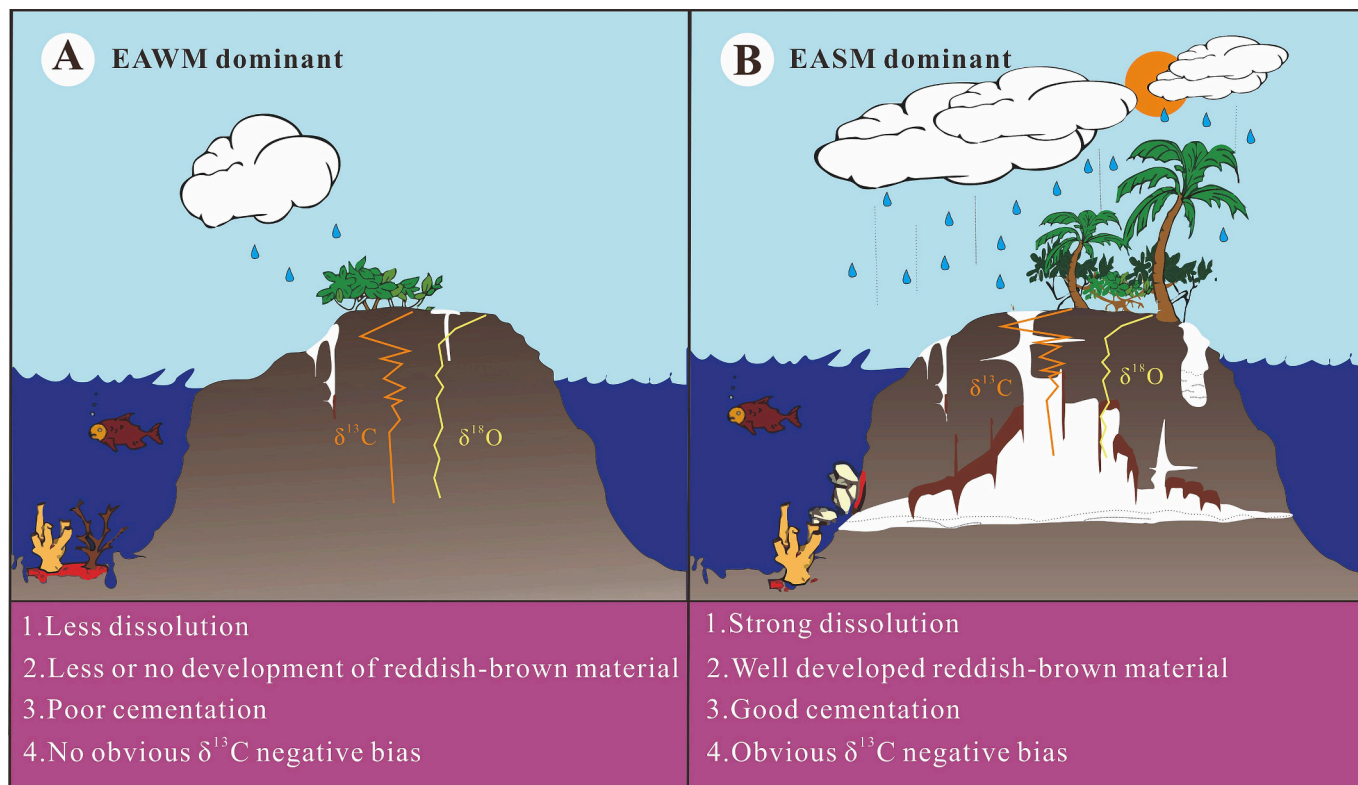

Fig. 10. Schematic diagram showing the diagenetic characteristics of the Pleistocene carbonate succession of CK-2 influenced by the (A) East Asian Winter Monsoon (EAWM) and (B) East Asian Summer Monsoon (EASM).

diagenesis of the rocks was controlled by the relative intensity of the East Asian Summer Monsoon. The Mid-Pleistocene Transition at ~0.9 ± 0.1 Ma, saw a strengthening of the East Asian Summer Monsoon that resulted in thick iron oxide layers, intensive dissolution, and extremely negative $\delta^{13}C$ values. In contrast, during low sea-level periods ~2 ± 0.12 Ma, ~0.3 ± 0.06 Ma, and ~ 7900 ± 70 a, meteoric diagenesis was less significant due to decreased intensity of the East Asian Summer Monsoon. The effects of East Asian Summer Monsoon on meteoric diagenesis of the Xisha platform can be traced back to the Pleistocene, suggesting that carbonate platforms can preserve monsoon signatures.

Declaration of Competing Interest

The authors declare that they have no known competing financial interests or personal relationships that could have appeared to influence the work reported in this paper.

Data availability

Data will be made available on request.

Acknowledgements

Appendix A. Supplementary data

Supplementary data to this article can be found online at https://doi.org/10.1016/j.palaeo.2023.111882.

References

Al-Ramadan, K., 2021. The role of diagenesis at unconformities of the Paleozoic siliciclastic succession of central Saudi Arabia: Implications for reservoir quality. Arab. J. Geosci. 14, 484–496.

Allan, J.R., Matthews, R.K., 1977. Carbon and oxygen isotopes as diagenetic and stratigraphic tools: Surface and subsurface data, Barbados, West Indies. Geology 5, 16–20.

Allan, J.R., Matthews, R.K., 1982. Isotope signatures associated with early meteoric diagenesis. Sedimentology 29, 797–817.

André, S., Strohmenger, C., 2010. Early diagenesis in Pleistocene coral reefs, southern Sinai, Egypt: response to tectonics, sea-level and climate. Sedimentology 44, 537–558.

Azmy, K., Brand, U., Sylvester, P., Gleeson, S.A., Logan, A., Bitner, M.A., 2011. Biogenic and abiogenic low-Mg calcite (bLMC and aLMC): Evaluation of seawater-REE composition, water masses and carbonate diagenesis. Chem. Geol. 280 (1–2), 180–190.

Azmy, K., Poty, E., Brand, U., 2009. High-resolution isotope stratigraphy of the Devonian-Carboniferous boundary in the Namur-Dinant Basin, Belgium. Sediment. Geol. 216, 117–124. https://doi.org/10.1016/j.sedgeo.2009.03.002.

Banner, J.L., 1995. Application of the trace element and isotope geochemistry of strontium to studies of carbonate diagenesis. Sedimentology 42, 805–824.

Berends, C.J., de Boer, S., van de Wal, R.S.W., 2021. Reconstructing the evolution of ice sheets, sea level, and atmospheric CO2 during the past 3.6 million years. Clim. Past 17, 361–377. https://doi.org/10.5194/cp-17-361-2021.

Bishop, J.W., Osleger, D.A., Montañez, I.P., Sumner, D.Y., 2014. Meteoric diagenesis and fluid-rock interaction in the Middle Permian Capitan backreef: Yates Formation, Slaughter Canyon, New Mexico. AAPG Bull. 98, 1495–1519.

Bonatti, E., Gartner, S., 1973. Caribbean climate during Pleistocene Ice Ages. Nature 244, 563–565.

Braithwaite, C.J.R., Montaggioni, L.F., 2009. The Great Barrier Reef: a 700000-year diagenetic history. Sedimentology 56, 1591–1622.

Braithwaite, C.J.R., Camoin, G.F., 2011. Diagenesis and sea-level change: lessons from Moruroa, French Polynesia. Sedimentology 58, 259–284.

Brand, U., Veizer, J., 1980. Chemical diagenesis of a multi-component carbonate system-1. J. Sediment. Petrol. 50, 1219–1236.

Budd, D.A., 1988. Petrographic products of freshwater diagenesis in Holocene ooid sands, Schooner Cays, Bahamas. Carbonat. Evapor. 3, 143–163.

Chen, J., Wang, H.T., 1996. Behaviours of Ree and other trace elements during pedological weathering-evidence from chemical leaching of loess and paleosol from the Luochuan section in central China. Acta Geol. Sin. 9, 290–302.

Chen, W.L., Wu, S.G., Huang, X.X., Liu, G., Han, X.H., 2020. Geochemical signatures in the Late Quaternary meteoric diagenetic carbonate succession, Xisha Islands, South China Sea. Acta Sedimentol. Sin. 38, 1296–1312 (in Chinese with English abstract).

Cheng, X., Zhao, Q., Wang, J., Jian, Z., Xia, P., Huang, B., Fang, D., Jian, X., Zhen, Z., Wang, P., 2004. (Table T1) Oxygen and carbon isotope ratios of planktic foraminifers from ODP Sites 184–1147 and 184–1148. Pangaea. https://doi.org/10.2973/odp.proc.sr.184.223.2004.

Christl, M., Lachner, J., Vockenhuber, C., Lechtenfeld, O., Stimac, I., Loeff, M., Synal, H. A., 2012. A depth profile of uranium-236 in the Atlantic Ocean. Geochim. Cosmochim. Acta 77, 98–107.

Clift, P.D., Wan, S., Blusztajn, J., 2014. Reconstructing chemical weathering, physical erosion and monsoon intensity since 25 Ma in the northern South China Sea: a review of competing proxies. Earth Sci. Rev. 130, 86–102.

Damuth, J.E., Fairbridge, R.W., 1970. Equatorial Atlantic deep-sea arkosic sands and Ice-Age aridity in Tropical South America. Geol. Soc. Am. Bull. 81, 189–206.

Della Porta, G.D., Webb, G.E., McDonald, I., 2015. REE patterns of microbial carbonate and cements from Sinemurian (Lower Jurassic) siliceous sponge mounds (Djebel Bou Dahar, High Atlas, Morocco). Chem. Geol. 400, 65–86.

Derry, L.A., Kaufman, A.J., Jacobsen, S.B., 1992. Sedimentary cycling and environmental change in the late Proterozoic: Evidence from stable and radiogenic isotopes. Geochim. Cosmochim. Acta 56, 1317–1329. https://doi.org/10.1016/0016-7037(92)90064-P.

Derry, L.A., Brasier, M.D., Corfield, R.M., Rozanov, A.Y., Zhuravlev, A.Y., 1994. Sr and C isotopes in Lower Cambrian carbonates from the Siberian craton: a paleoenvironmental record during the 'Cambrian explosion'. Earth Planet. Sci. Lett. 128, 671–681.

Dehler, C.M., Elrick, M., Bloch, J.D., Crossey, L.J., Karlstrom, K.E., Marais, D.J.D., 2005. High-resolution δ13C stratigraphy of the Chuar Group (ca. 770–742 Ma), Grand Canyon: Implications for Mid-Neoproterozoic climate change. Geol. Soc. Am. Bull. 117, 32–45.

Ding, Z., Yu, Z., Rutter, N.W., Liu, T., 1994. Towards an orbital time-scale for Chinese loess deposits. Quat. Sci. Rev. 13, 39–70.

Emiliani, C., 1970. Pleistocene temperatures. Science 168, 822–825.

Fan, T.L., Yu, K.F., Zhao, J.X., Jiang, W., Xu, S.D., Zhang, Y., Wang, R., 2020. Strontium isotope stratigraphy and paleomagnetic age constraints on the evolution history of coral reef islands, northern South China Sea. Geol. Soc. Am. Bull. 132, 813–816.

Fantle, M.S., Barnes, B.D., Lau, K.V., 2020. The Role of Diagenesis in Shaping the Geochemistry of the Marine Carbonate Record. Annu. Rev. Earth Planet. Sci. 48 (1), 549–583.

Gai, C., Liu, Q., Roberts, A.P., 2020. East Asian monsoon evolution since the late Miocene from the South China Sea. Earth Planet. Sci. Lett. 530, 115960.

Guo, Z.T., Ruddiman, W.F., Hao, Q.Z., Wu, H.B., Qiao, Y.S., Zhu, R.X., Peng, S.Z., Wei, J. J., Yuan, B.Y., Liu, T.S., 2002. Onset of Asian desertification by 22 Myr ago inferred from loess deposits in China. Nature 416, 159.

Halley, R.B., Harris, P.M., 1979. Fresh-water cementation of a 1,000-year-old oolite. J. Sediment. Petrol. 49, 969–987.

Harrison, R.S., 1975. Porosity in Pleistocene grainstones from Barbados: some preliminary observations. Bull. Can. Petrol. Geol. 23, 383–392.

Haq, B.U., Hardenbol, J., Vail, P.R., 1988. Mesozoic and Cenozoic chronostratigraphy and cycles of sea-level change. Integrated Approach 7–108.

Hongbo, Zheng, Powell, Christopher, Mcaulay, 2000. Pliocene uplift of the northern Tibetan Plateau. Geology 28 (8), 715–718.

Hu, J.Y., Kawamura, H., Hong, H.S., Qi, Y.Q., 2000. A Review on the currents in the South China Sea: seasonal circulation, South China Sea warm current and Kuroshio intrusion. J. Oceanogr. 56, 607–624.

Huang, C.Y., Wu, S.F., Zhao, M., Chen, M.T., Yuan, P.B., 1997. Surface ocean and monsoon climate variability in the South China Sea since the last glaciation. Mar. Micropaleontol. 32, 71–94.

Huang, B., Jian, Z., Cheng, X., Wang, P., 2003. Foraminiferal responses to upwelling variations in the South China Sea over the last 220 000 years. Mar. Micropaleontol. 47 (1–2), 1–15.

Huang, B., Jian, Z., Wang, P., 2005. Palaeoceanographic evolution recorded in the northern South China Sea since 4 Ma. Sci. China 48 (12), 2166–2173.

Huang, S.J., 2010. In: Carbonate Diagenesis. Geological publishing house, Beijing, pp. 1–288 (in Chinese with English abstract).

Huang, R.H., Chen, J.L., Wang, L., Lin, Z.D., 2012. Characteristics, processes, and causes of the spatio-temporal variabilities of the East Asian monsoon system. Adv. Atmos. Sci. 29 (5), 910–942.

Jia, G., Peng, P., Zhao, Q., Jian, Z., 2003. Changes in terrestrial ecosystem since 30 Ma in East Asia: stable isotope evidence from black carbon in the South China Sea. Geology 31, 1093–1096.

Jian, Z., Zhao, Q., Cheng, X., Wang, J., Wang, P., Xin, S., 2003. Pliocene-Pleistocene stable isotope and palaeoceanographic changes in the northern South China Sea. Paleogeogr. Palaeoclimatol. Palaeoecol. 193, 425–442.

Jiang, W., Yu, K., Song, Y., Zhao, J.X., Feng, Y.X., Wang, Y., Xu, S., Han, T., 2018. Annual REE signal of East Asian Winter Monsoon in surface seawater in the northern South

China Sea: Evidence from a century-long Porites coral record. Paleoceanogr. Paleoclimatol. 33, 168–178.

Jiang, W., Yu, K.F., Fan, T.L., Xu, S.D., Wang, R., Zhang, Y., Yue, Y.F., Zhao, J.X., Feng, Y.X., Wei, C.S., Wang, S.P., Wang, Y.H., 2019. Coral reef carbonate record of the Pliocene-Pleistocene climate transition from an atoll in the South China. Marine Geol. 411, 88–97.

Jones, B., 2016. Cave-fills in Miocene-Pliocene strata on Cayman Brac, British West Indies: Implications for the geological evolution of an isolated oceanic island. Sediment. Geol. 341, 70–95.

Kamber, W., Webb, G.E., 2000. Rare earth elements in Holocene reefal microbialites: a new shallow seawater proxy. Geochim. Cosmochim. Acta 64, 1557–1565.

Kaufman, A.J., Jacobsen, S.B., Knoll, A.H., 1993. The Vendian record of Sr and C isotopic variations in seawater: Implications for tectonics and paleoclimate. Earth Planet. Sci. Lett. 120, 409–430.

Kaufman, A.J., Knoll, A.H., 1995. Neoproterozoic variations in the C-isotopic composition of seawater: stratigraphic and biogeochemical implications. Precambr. Res. 73, 27–49.

Kuang, Z.G., Guo, Y.Q., Wang, L.L., Liang, J.Q., Sha, Z.B., 2014. Evolution of the Late Miocene atoll systems offshore Xisha Islands. Sci. China Earth Sci. 57, 3084–3096.

Li, B., Wang, J., Huang, B., Li, Q., Jian, Z., Zhao, Q., Su, X., Wang, P., 2004. South China Sea surface water evolution over the last 12 Myr: A south-north comparison from Ocean Drilling Program Sites 1143 and 1146. Paleoceanography 19, PA1009.

Li, R., Jones, B., 2013. Temporal and spatial variations in the diagenetic fabrics and stable isotopes of Pleistocene corals from the Ironshore Formation of Grand Cayman, British West Indies. Sediment. Geol. 286–287, 58–72.

Li, R., Qiao, P.J., Cui, Y.C., Zhang, D.J., Liu, X.Y., Shao, L., 2018. Composition and diagenesis of Pleistocene aeolianites at Shidao, Xisha Islands: Implications for paleoceanography and paleoclimate during the last glacial period. Paleogeogr. Palaeoclimatol. Palaeoecol. 490, 604–616.

Liu, J., Han, C.R., Wu, J.Z., Ju, L.J., 1998a. Geochemical evidence for the meteoric diagenesis in Pleistocene reef limestones of Xisha Islands. Acta Sedimentol. Sin. 4, 71–77.

Liu, T.S., Zheng, M.P., Guo, Z.T., 1998b. Initiation and evolution of the Asian monsoon system timely coupled with the ice-sheet growth and the tectonic movements in Asia. Quat. Sci. 3, 194–204.

Liu, Z., Colin, C., Huang, W., Le, K.P., Tong, S., Chen, Z., Trentesaux, A., 2007. Climatic and tectonic controls on weathering in South China and Indochina Peninsula: clay mineralogical and geochemical investigations from the Pearl, Red, and Mekong drainage basins. Geochem. Geophys. Geosyst. 8 https://doi.org/10.1029/2006GC001490.

Lu, J., Yang, H., Griffiths, M.L., Burls, N.J., Xiao, G.Q., Yang, J.L., Wang, J.K., Johnson, K.R., Xie, S.C., 2021. Asian monsoon evolution linked to Pacific temperature gradients since the Late Miocene. Earth Planet. Sci. Lett. 563 (1), 116882.

Luo, Y., Li, G., Xu, W.H., Liu, J.G., Cheng, J., Zhao, J.X., Yan, W., 2021b. The effect of diagenesis on rare earth element geochemistry of the Quaternary carbonates at an isolated coral atoll in the South China Sea. Sediment. Geol. 420, 105933.

Luo, Y., Li, G., Xu, W.H., Cheng, J., Liu, J.G., Yan, W., 2022. Characteristics of Quaternary exposure surfaces in Well Nanke 1 and its relationship with sea level changes. J. Trop. Oceanogr. 41, 143–157 (in Chinese with English abstract).

Ma, Y., Wu, S., Lv, F., Dong, D., Gu, M., 2011. Seismic characteristics and development of the Xisha carbonate platforms, northern margin of the South China Sea. J. Asian Earth Sci. 40, 770–783.

Ma, Y., Qin, Y., Yu, K., Li, Y., Long, Y., Wang, R., Fan, T., Jiang, W., Xu, S., Zhao, J., 2021. Holocene coral reef development in Chenhang Island, Northern South China Sea, and its record of sea level changes. Mar. Geol. 440, 106593.

Martin, G.D., Wilkinson, B.H., Lohmann, K.C., 1986. The role of skeletal porosity in aragonite neomorphism-Strombus and Montastrea from the Pleistocene Key Largo limestone, Florida. J. Sediment. Petrol. 56, 194–203.

Matthews, R.K., 1968. Carbonate Diagenesis: Equilibration of Sedimentary Mineralogy to the Subaerial Environment; Coral Cap of Barbados, West Indies. J. Sediment. Res. 38 (2), 113–115.

Matthews, R.K., Frohlich, C., 1987. Forward modeling of bank-margin carbonate diagenesis. Geology 15 (7), 673–676.

McGregor, H.V., Gagan, M.K., 2003. Diagenesis and geochemistry of Porites corals from Papua New Guinea: Implications for paleoclimate reconstruction. Geochim. Cosmochim. Acta 67, 2147–2156.

Molnar, P, Boos, W R, Battisti, D S, 2010. Orographic Controls on Climate and Paleoclimate of Asia: Thermal and Mechanical Roles for the Tibetan Plateau. Annual Rev. Earth Planet. Sci. 38 (1), 77–102. https://doi.org/10.1146/annurev-earth-040809-152456.

Qiao, P.J., Zhu, W.L., Shao, L., Zhang, D.J., Cheng, X.R., Song, Y.M., 2015. Carbonate stable isotope stratigraphy of Well Xike-1, Xisha Islands. Earth Sci.J. China Univ. Geosci. 40, 725–732 (in Chinese with English abstract).

Qin, Y.M., Yu, K.F., Wang, R., Jiang, W., Xu, S.D., 2019. The initiation time of the Holocene coral reef at the Chenhang Island (Xisha Islands) and its significance as a sea level indicator. Trop. Geogr. 39, 319–328 (in Chinese with English abstract).

Rao, C.P., 1991. Geochemical differences between subtropical (Ordovician), cool temperate (Recent and Pleistocene) and subpolar (Permian) carbonates, Tasmania, Australia. Carbonat. Evapor. 6, 83–106.

Rea, D.K., Snoeckx, H., Joseph, L.H., 1998. Late Cenozoic Eolian deposition in the North Pacific: Asian drying, Tibetan uplift, and cooling of the northern hemisphere. Paleoceanography 13, 215–224.

Ren, M., Jones, B., 2016. Diagenesis in limestone-dolostone successions after 1 million years of rapid sea-level fluctuations: A case study from Grand Cayman, British West Indies. Sediment. Geol. 342, 15–30.

Rightmire, C.T., Hanshaw, B.B., 1973. Relationship between the carbon isotope composition of soil CO2 and dissolved carbonate species in groundwater. Water Resour. Res. 9, 958–967.

Saller, A.H., Moore, C.H., 1989. Meteoric diagenesis, marine diagenesis, and microporosity in Pleistocene and Oligocene limestones, Enewetak Atoll, Marshall Islands. Sediment. Geol. 63, 253–272.

Shao, L., Li, Q.Y., Zhu, W.L., Zhang, D.J., Qiao, P.J., Liu, X.Y., You, L., Cui, Y.C., Dong, X.X., 2017a. Neogene carbonate platform development in the NW South China Sea: Litho-, bio- and chemo-stratigraphic evidence. Mar. Geol. 385, 233–243.

Shao, L., Cui, Y., Qiao, P., Zhang, D., Liu, X., Zhang, C., 2017b. Sea-level changes and carbonate platform evolution of the Xisha Islands (South China Sea) since the Early Miocene. Paleogeogr. Palaeoclimatol. Palaeoecol. 485, 504–516.

Song, Y., Fang, X., Li, J., An, Z., Miao, X., 2001. The Late Cenozoic uplift of the Liupan Shan, China. Sci. China Ser. D 44, 176–184 (in Chinese with English abstract).

Steinke, S., Groeneveld, J., Johnstone, H., Rendle-Bühring, R., 2010. East Asian summer monsoon weakening after 7.5 Ma: evidence from combined planktonic foraminifera Mg/Ca and δ18O (ODP Site 1146; northern South China Sea). Paleogeogr. Palaeoclimatol. Palaeoecol. 289 (1–4), 33–43.

Sun, Y., Wang, T., Yin, Q., Lyu, A., Crucifix, M., Cai, Y., Ai, L., Clemens, S., An, Z., 2022. A review of orbital-scale monsoon variability and dynamics in East Asia during the Quaternary. Quat. Sci. Rev. 288, 107593.

Swart, P.K., 2015. The geochemistry of carbonate diagenesis: The past, present and future. Sedimentology 62, 1233–1304.

Swart, P.K., Oehlert, A.M., 2018. Revised interpretations of stable C and O patterns in carbonate rocks resulting from meteoric diagenesis. Sediment. Geol. 364, 14–23.

Siahi, M., Hofmann, A., Master, S., Wilson, A., Mayr, C., 2018. Trace element and stable (C, O) and radiogenic (Sr) isotope geochemistry of stromatolitic carbonate rocks of the Mesoarchean Pongola Supergroup: Implications for seawater composition. Chem. Geol. 476, 389–406.

Wan, S.M., 2006. Evolution of the East Asian monsoon: Mineralogical and sedimentologic records in the south China sea since 20 Ma. Thesis. In: Institute of Oceanology, Chinese Academy of Sciences, pp. 1–171 (in Chinese with English abstract).

Wan, S., Li, A., Clift, P.D., Stuut, J.B.W., 2007. Development of the East Asian monsoon: mineralogical and sedimentological records in the northern South China Sea since 20 Ma. Palaeogeogr. Palaeoclimatol. Palaeoecol. 254, 561–582.

Wang, R., Yu, K.F., Jones, B., Wang, Y.H., Zhao, J.X., Feng, Y.X., Bian, L.Z., Xu, S.D., Fan, T.L., Jiang, W., Zhang, Y., 2018. Evolution and development of Miocene "island dolostones" on Xisha islands, South China Sea. Marine Geol. 406, 142–158.

Webb, G.E., Nothdurft, L.D., Kamber, B.S., Kloprogge, J.T., Zhao, J.X., 2009. Rare earth element geochemistry of scleractinian coral skeleton during meteoric diagenesis: a sequence through neomorphism of aragonite to calcite. Sedimentology 56, 1433–1463.

Whitaker, F.F., 1997. Hydrogeology of the Bahamian Archipelago. Geol. Hydrogeol. Carbonate Islands.

Wu, F., Xie, X.N., Betzler, C., Zhu, W.L., Zhu, Y.H., Guo, L.Y., Ma, Z.L., Bai, H.Q., Ma, B.J., 2019. The impact of eustatic sea-level fluctuations, temperature variations and nutrient-level changes since the Pliocene on tropical carbonate platform (Xisha Islands, South China Sea). Paleogeogr. Palaeoclimatol. Palaeoecol. 514, 373–385.

Wu, F., Xie, X., Zhu, Y., Coletti, G., Betzler, C., Cui, Y., Bai, H., Chen, B., Shang, Z., 2021. Early development of carbonate platform (Xisha Islands) in the northern South China Sea. Mar. Geol. 441, 106629.

Xu, S., Yu, K., Fan, T., Jiang, W., Wang, S., 2019. Coral reef carbonate δ13C records from the northern South China Sea: A useful proxy for seawater δ13C and the carbon cycle over the past 1.8 Ma. Glob. Planet. Chang. 182, 103003.

Yang, Z., Zhang, G.X., Zhang, L., Xia, B., 2016. Development and controlling factors of Neogene reefs in Xisha Sea area. Pet. Geol. Exp. 38, 787–795 (in Chinese with English abstract).

Yang, Y., Yu, K., Wang, R., Fan, T., Jiang, W., Xu, S., Li, Y., Zhao, J., 2022. 87Sr/86Sr of coral reef carbonate strata as an indicator of global sea level fall: Evidence from a 928.75-m-long core in the South China Sea. Mar. Geol. 445, 106758.

You, L., Yu, Y.P., Liao, J., Liu, L., Liu, N., Zhao, S., Li, X., 2015. Petrological characteristics and pore types of Quaternary reef adjacent typical exposed surface in Well Xike-1, Xisha Islands. Earth Sci.J. China Univ. Geosci. 4, 6.

Zhang, Y., Yu, K.F., Qian, H.D., Fan, T.L., Yue, Y.F., Wang, R., Jiang, W., Xu, S.D., Wang, Y.H., 2020. The basement and volcanic activities of the Xisha Islands: Evidence from the kilometer-scale drilling in the northwestern South China Sea. Geol. J. 55, 571–583.

Zhang, Z., Licht, A., De Vleeschouwer, D., Wang, Z., Li, Y., Kemp, D.B., Tan, L.C., Zhang, R., Qiang, X.K., Huang, C.J., 2022. East Asian monsoonal climate sensitivity changed in the late Pliocene in response to Northern Hemisphere glaciations. Geophys. Res. Lett. 49, e2022GL101280.

Zhao, Q., 2010. The sedimentary research about reef carbonatite in Xisha Island waters. Thesis. In: Institute of Oceanology, Chinese, pp. 1–169 (in Chinese with English abstract).

Zhao, Q., Wu, S., Xu, H., Sun, Q., Wang, B., Sun, Y., Cao, F., He, X., 2011. Sedimentary facies and evolution of aeolianites on Shidao Island, Xisha Islands. China J. Oceanogr. Limnol. 29, 398–413.

Zhu, W.L., Wang, Z.F., Mi, L.J., Du, X.B., Xie, X.N., Lu, Y.C., Zhang, D.J., Sun, Z.P., Liu, X.Y., You, L., 2015. Sequence stratigraphic framework and reef growth unit of well Xike-1 from Xisha Island, South China Sea. Earth Sci.-J. China Univ. Geosci. 40, 677–687 (in Chinese with English abstract).